Molecular basis for activation of lecithin:cholesterol acyltransferase by a compound that increases HDL cholesterol

Kelly A. Manthei[1], Shyh-Ming Yang[2], Bolormaa Baljinnyam[2], Louise Chang[1], Alisa Glukhova[1], Wenmin Yuan[3], Lita A. Freeman[4], David J. Maloney[2], Anna Schwendeman[3], Alan T. Remaley[4], Ajit Jadhav[2], and John J.G. Tesmer[*5]

[1]Life Sciences Institute, University of Michigan, Ann Arbor, Michigan 48109, United States

[2]National Center for Advancing Translational Sciences, National Institutes of Health, Rockville, Maryland 20850, United States

[3]Department of Pharmaceutical Sciences and Biointerfaces Institute, University of Michigan, Ann Arbor, Michigan 48109, United States

[4]Lipoprotein Metabolism Section, Cardiovascular-Pulmonary Branch, National Heart, Lung, and Blood Institute, National Institutes of Health, Bethesda, Maryland 20814, United States

[5]Department of Biological Sciences, Purdue University, West Lafayette, Indiana 47907, United States

[*]To whom correspondence should be addressed: jtesmer@purdue.edu

ABSTRACT

Lecithin:cholesterol acyltransferase (LCAT) and LCAT-activating small molecules are being investigated as treatments for coronary heart disease (CHD) and familial LCAT deficiency (FLD). Herein we report the crystal structure of LCAT bound to a potent activator and an acyl intermediate-like inhibitor, thereby revealing an active conformation of LCAT and that the activator is bound exclusively to its membrane-binding domain (MBD). Functional studies indicate that the compound does not modulate the affinity of LCAT for HDL, but instead stabilizes residues in the MBD and likely facilitates channeling of substrates into the active site. By demonstrating that these activators increase the activity of an FLD variant, we show that compounds targeting the MBD have therapeutic potential. In addition, our data better define the acyl binding site of LCAT and pave the way for rational design of LCAT agonists and improved biotherapeutics for augmenting or restoring reverse cholesterol transport in CHD and FLD patients.

Coronary heart disease (CHD) is the leading cause of death in the world and typically develops as the result of atherosclerotic plaque build-up in the arteries. Risk for CHD is inversely related to high-density lipoprotein (HDL) cholesterol (HDL-C) levels in plasma. In reverse cholesterol transport (RCT), HDL receives cholesterol from cholesterol-enriched macrophages, which is then esterified by lecithin:cholesterol acyltransferase (LCAT) bound to HDL. LCAT preferentially catalyzes hydrolysis of the *sn*-2 acyl group from phosphatidylcholine (lecithin) and its transfer to cholesterol, creating a cholesteryl ester (CE), which partitions to the hydrophobic core of the HDL particle (Calabresi et al., 2012). This process drives the maturation of discoidal pre-β HDL to spherical α-HDL and promotes further cholesterol efflux from arterial plaques (Glomset, 1968).

LCAT esterification of cholesterol in HDL is promoted by ApoA-I, the most abundant structural apolipoprotein in HDL (Fielding et al., 1972; Jonas, 2000). The structural determinants that underlie ApoA-I activation of LCAT are poorly understood, but some clues have been provided by a series of crystal structures of LCAT (Gunawardane et al., 2016; Manthei et al., 2017; Piper et al., 2015) and the closely-related lysosomal phospholipase A2 (LPLA2) (Glukhova et al., 2015). Both enzymes contain an α/β-hydrolase domain and two accessory domains referred to as the membrane-binding domain (MBD) and cap domain. The MBD contains hydrophobic residues important for LPLA2 to bind liposomes and for LCAT to bind HDLs. Protruding from the cap domain is an active site lid that has been observed in multiple conformations. In the case of LCAT, crystallographic and hydrogen/deuterium exchange mass spectrometry (HDX MS) studies suggest that the lid blocks the active site in its inactive state, and opens in response to the binding of substrates and, presumably, upon interaction with HDL (Manthei et al., 2017). The lid

region is also important for HDL-binding (Cooke et al., 2018; Glukhova et al., 2015; Manthei et al., 2017), and thus we hypothesize that activation imposed by ApoA-I involves conformational changes in LCAT that stabilize its lid in an open state that is more competent to bind substrates.

To date, over 90 genetic mutations in LCAT have been described and are responsible for two phenotypes of LCAT deficiency: fish eye disease (FED), wherein patients retain residual LCAT activity, particularly on apoB-containing lipoproteins, and familial LCAT deficiency (FLD), wherein patients exhibit a total loss of LCAT activity (Kuivenhoven et al., 1997; Rousset et al., 2009). Both are characterized by low levels of HDL-C and corneal opacities, but FLD presents additional serious symptoms including anemia, proteinuria, and progressive renal disease, the main cause of morbidity and mortality in these patients (Ahsan et al., 2014; Ossoli et al., 2016; Rousset et al., 2011). Novel treatments for raising HDL-C largely based on cholesteryl ester transfer protein inhibition have failed to protect against CHD in clinical trials (Kingwell et al., 2014; Rader, 2016). Therefore, there is currently great interest in investigating alternative pathways for modulating HDL metabolism. In particular, the focus has switched from raising HDL-C to developing drugs that increase the beneficial properties of HDL, such as cholesterol efflux, which is enhanced by LCAT (Czarnecka and Yokoyama, 1996). New treatments that increase LCAT activity could therefore be beneficial for both FLD and CHD patients.

Recombinant human LCAT (rhLCAT), which raises HDL-C and increases cholesterol efflux, was shown to be safe in a phase I study (Shamburek et al., 2016b) and is now in phase II trials for CHD. This same rhLCAT has also been tested in enzyme replacement therapy for one patient with FLD with encouraging results (Shamburek et al., 2016a). However, small molecule activators would be less expensive and easier to administer than a biotherapeutic. Previously,

Amgen identified Compound A (3-(5-(ethylthio)-1,3,4-thiadiazol-2-ylthio)pyrazine-2-carbonitrile)), which binds covalently to Cys31 in the active site of LCAT and increases plasma CE and HDL-C levels in mice and hamsters (Chen et al., 2012; Freeman et al., 2017; Kayser et al., 2013). Other sulfhydryl-reactive compounds based on monocyclic β-lactams have also been shown to activate LCAT (Freeman et al., 2017). Although highlighting the promise of LCAT-activating molecules, these compounds are expected to have many off-target effects. Recently, Daiichi Sankyo reported a new class of reversible small molecule activators that have demonstrated the ability to activate LCAT isolated from human plasma (Kobayashi et al., 2016; Kobayashi et al., 2015a; Kobayashi et al., 2015b; Onoda et al., 2015), and increased HDL-C up to 1000-fold when orally administered to cynomolgus monkeys (Onoda et al., 2015).

Here we determined the structure of LCAT bound to both a Daiichi Sankyo piperidinylpyrazolopyridine activator and isopropyl dodecyl fluorophosphonate (IDFP), a covalent inhibitor that mimics an acylated reaction intermediate, in which the enzyme adopts an active conformation with an open lid. The activator binds in a pocket formed exclusively by the MBD but does not influence affinity of LCAT for HDL. The lid, which contains positions mutated in FLD, undergoes a large conformational change from that observed in inactive LCAT structures. We show that variants of Arg244 within the lid recover acyltransferase activity when treated with a piperidinylpyrazolopyridine activator, highlighting the promise of compounds that target the MBD for many missense FLD variants. Our results provide a better understanding of the key conformational changes that LCAT undergoes during activation, insight into how the enzyme alters its conformation in response to acyl substrates, and a rational framework for the design of new small molecule LCAT modulators.

RESULTS

Characterization of LCAT activators

We first synthesized and confirmed the ability of three recently reported piperidinylpyrazolopyridine and piperidinylimidazopyridine LCAT activators (Kobayashi et al., 2015a; Onoda et al., 2015) (compounds **1**-**3**, Figure 1a) to activate hydrolysis of 4-methylumbelliferyl palmitate (MUP) by full-length LCAT (Figure 1b). All three activated LCAT greater than 2-fold, with EC_{50} values of 160, 280 and 320 nM for **1**, **2**, and **3**, respectively (Table 1, 2). We also examined the acyltransferase activity of LCAT with dehydroergosterol (DHE) incorporated in peptide-based HDLs in response to compound **2**, as it has lower background fluorescence in this assay. We observed that **2** activates LCAT 2.8-fold with an EC_{50} of 280 nM (Table 1, Figure 1c). To gain insight into the mechanism of activation, we determined the V_{max} and K_m values for the DHE assay with and without 5 μM compound **2**. The V_{max} increased from 22 to 37 μM DHE-ester hr^{-1}, whereas the K_m was not significantly changed (11 μM vs. 6.6 μM with **2**) (Figure 1d).

We next examined the ability of compound **1** to modulate HDL-binding by pre-incubating the compound with LCAT and then monitoring the kinetics of LCAT binding to ApoA-I HDLs with bio-layer interferometry (BLI). There was no change in the k_{on}, k_{off}, or overall K_d in BLI, and thus the compounds do not appear to act by increasing LCAT affinity for HDL (Table 3, Figure 1e, S1a). The activators did however increase the melting temperature (T_m) of LCAT (ΔT_m from values of 2.7 – 5.0 ˚C), similar to that which occurs upon reaction of LCAT with isopropyl dodecyl fluorophosphonate (IDFP) (ΔT_m = 7 ˚C) (Manthei et al., 2017) (Figure 1f-g). A K_d value of 100 ± 14 nM was determined for compound **1** binding to LCAT via microscale thermophoresis (MST) (Figure S1b).

123 **Structure of activated LCAT**

124 With the goal of visualizing an active conformation of LCAT, we examined the combined ability
125 of both **1** and IDFP to stabilize ΔNΔC-LCAT (residues 21-397), a truncation variant that lacks
126 the dynamic N- and C-termini of the enzyme and thus is more readily crystallized (Glukhova et
127 al., 2015; Gunawardane et al., 2016; Manthei et al., 2017; Piper et al., 2015). The ligands had an
128 additive effect (ΔT_m of 12.7 ˚C), suggesting that the two ligands have distinct, non-overlapping
129 binding sites (Figure 1f-g). Because increased protein stability improves the chances of obtaining
130 crystals, ΔNΔC-LCAT incubated with both IDFP and **1** (ΔNΔC-IDFP·**1**) was thus subjected to
131 crystallization trials. An additional benefit was that the ligands were also expected to also trap an
132 active conformation of LCAT. The resulting structure was determined using diffraction data to
133 3.1 Å spacings (Figure 2, Table 4). Crystals could not be obtained without both ligands. There
134 are two protomers of ΔNΔC-IDFP·**1** in the asymmetric unit with a root mean square deviation
135 (RMSD) of 0.35 Å for all Cα atoms, indicating nearly identical conformations (Krissinel and
136 Henrick, 2004). Density was observed for residues spanning 21-397 of chain A and 21-395 of
137 chain B, although in both chains a portion of the lid is disordered (239-240 in chain A and 236-
138 242 in chain B).
139
140 Strong omit map density is observed for both **1** and portions of IDFP (Figure 2b, d). Compound **1**
141 binds in a groove formed by the MBD of each subunit, burying 380 $Å^2$ of accessible surface area
142 of the protein (Pettersen et al., 2004) (Figure 2b-c). The bicyclic head of **1** binds in a pocket
143 chiefly formed by the b1-b2 loop and a1 and a2 helices (nomenclature as in LPLA2 (Glukhova et
144 al., 2015)), including the Cys50-Cys74 disulfide bond (Figure 2a-c). Its pyrazole ring donates
145 and accepts a hydrogen bond with the backbone carbonyl and amide of Met49 and Tyr51,

146 respectively, which mandates the hydrogen to be on the 2-position of the ring (Figure S2a,
147 Compound **1-b**). The C4 hydroxyl donates a hydrogen bond to the side chain of Asp63, and the
148 C6 carbonyl accepts a hydrogen bond from the side chain of Asn78. The C4 trifluoromethyl
149 group is buried against the a1 and a2 helices. Thus, although compound **1** was synthesized as a
150 racemic mixture at the C4 position, the binding site is only compatible with the ***R*** enantiomer
151 (Figure S2a, Compound **1-c**). For simplicity, in future descriptions the compound in the structure
152 is still referred to as compound **1**. The stereochemical preference is consistent with previous
153 observations that one optical enantiomer of a given activator is typically at least ten-fold more
154 potent than the other (Kobayashi et al., 2015a; Kobayashi et al., 2015b). The pyrazole moiety
155 packs between the side chain of Tyr51 and the Cys50-Cys74 disulfide. The central piperidine
156 ring of **1** forms van der Waals contacts, but also positions the terminal pyrazine ring of **1** in a
157 hydrophobic cleft formed by the side chains of Met49, Leu68, Pro69, and Leu70 (Figure 2b).
158 One edge of the pyrazine moiety also participates in crystal lattice contacts with residues in the
159 αA-αA′ loop (residues 111-119), a region proposed to be involved in cholesterol binding
160 (Glukhova et al., 2015; Manthei et al., 2017), although these lattice contacts are distinct in each
161 chain (Figure S3a-b). This contact may explain why similar crystals could not be obtained with
162 compounds **2** and **3**, which have bulky trifluoromethyl substitutions for the pyrazine cyano
163 group.
164
165 Notably, the binding site for **1** is also occupied in some prior LCAT and LPLA2 crystal structures
166 (Figure 3a-b), either by a Phe-Tyr dipeptide of an inhibitory Fab fragment (Fab1) (PDB entries
167 4XWG, 4XX1, 5BV7) (Gunawardane et al., 2016; Piper et al., 2015) or by a HEPES molecule in
168 structures of LPLA2 (Glukhova et al., 2015), indicating that the MBD in the LCAT/LPLA2

family is a robust binding site for diverse chemical matter. Because the 4XWG and 4XX1 structures (referred to as LCAT–Fab1) of LCAT adopt what seems to be an inactive conformation (Manthei et al., 2017; Piper et al., 2015), general occupation of the activator binding site is however insufficient to trigger a global conformational transition in LCAT.

The strongest omit density for IDFP corresponds to its phosphonate head group, which is covalently bound to Ser181 and occupies the oxyanion hole (Figure 2d-e). The density is progressively weaker beyond the phosphonate, and the alkyl chain past the C2 carbon is not observed. However, the location of IDFP in our structure and the dynamic nature of the alkyl chain is consistent with results from the LPLA2-IDFP structure (PDB entry 4X91), wherein multiple conformations of bound IDFP revealed two hydrophobic tracks likely used for binding the acyl chains of phospholipid substrates (Glukhova et al., 2015) (Figure S3c). Indeed, there is a similar hydrophobic track corresponding to track A that takes a straighter path to the back of the LCAT as compared the one observed for LPLA2, which results from the different orientations of their lids (Figure S3b-c). We previously used HDX MS to show that IDFP stabilizes elements in the MBD and the lid region of LCAT (Manthei et al., 2017). This data is in agreement with what we observe in the crystal structure of ΔNΔC-IDFP·**1**, in that residues 67-72 in the MBD and residues 226-236 in the lid have markedly lower temperature factors in the structure reported here as compared to LCAT structures without IDFP (Figure S4).

Comparison with prior LCAT structures reveals a global conformational switch

Reported atomic structures of LCAT include that of full-length LCAT wherein its lid extends over and shields the active site (PDB entry 5TXF, LCAT-closed), LCAT in complex with

192 inhibitory Fab1 (LCAT–Fab1), and LCAT in complex with Fab1 and a second agonistic Fab
193 fragment (27C3) (entry 5BV7, 27C3–LCAT–Fab1; Figure 3c). In these structures, the N- and C-
194 termini are disordered except for an N-terminal pentapeptide in the 27C3–LCAT–Fab1 structure
195 (containing mutations L4F/N5D) that docks in the active site of a neighboring symmetry mate. It
196 is unclear which of these structures, if any, represent an activated conformation of LCAT,
197 although the LCAT–Fab1 and LCAT-closed structures are more similar to each other and likely
198 to be inactive, whereas 27C3–LCAT–Fab1 has a more exposed active site. The conformation of
199 the active site lid is highly variable among these three structures.
200
201 The ΔNΔC-IDFP·**1** structure affords a high-resolution view of LCAT in what is expected to be a
202 fully activated conformation unobstructed by conformational changes that might be induced by
203 Fab binding. The structure of LCAT here is most similar to that in 27C3–LCAT–Fab1 (RMSD
204 0.70 Å for all Cα atoms) (Gunawardane et al., 2016; Krissinel and Henrick, 2004), including in
205 their active site lid regions and in the relative configuration of their three domains (Figure S4a-
206 b). The active site lid can be divided into two regions, with the C-terminal portion (residues 233-
207 249) being most consistent between the two structures. Both structures contain similar disordered
208 segments (residues 236-242 in 27C3–LCAT–Fab1, chain A residues 239-240 and chain B
209 residues 236-242 in ΔNΔC-IDFP·**1**). The N-terminal portion of the lid (residues 225-232) is most
210 variable, although it is consistent between the two unique chains of the ΔNΔC-IDFP·**1** structure
211 and, given the substrate analog, more likely to adopt a physiological conformation. Indeed, the
212 N-terminal pentapeptide of a symmetry mate in the 27C3–LCAT–Fab1 structure would clash
213 with Asn228 in the lid region of ΔNΔC-IDFP·**1**. Regardless, such differences highlight the high

214 plasticity of the active site, which is likely required for LCAT to accommodate its various lipidic
215 substrates.
216
217 Comparison of the structure of LCAT-closed with ΔNΔC-IDFP·**1** provides a unique glimpse of
218 how LCAT transitions from inactive to active states (Movie S1). Domain motion analysis
219 (Hayward and Berendsen, 1998) reveals two hinge regions: residues 219-229 and 251-255
220 (Movie S2). The dihedral angles between Asn228-Gln229 and Gln229-Gly230 undergo a large
221 rotation that flips the lid region away from the active site in the ΔNΔC-IDFP·**1** complex. On the
222 other end of the lid, the α5 helix of the cap domain unwinds in the lid open state, with the
223 dihedral angles between Pro250-Trp251 undergoing the most change (Figure 3c-d, Movie S2).
224 The lid transition is accompanied by a 4˚ change in the orientation of the adjacent cap domain
225 relative to both the α/β-hydrolase and MBD, which remain fixed with respect to each other
226 (Figure 3c, Movie S1). Interestingly, in all reported LCAT structures the binding site for
227 compound **1** is accessible (with obvious exception of those in complex with Fab1, which takes
228 advantage of the same site), regardless of the orientation of the cap domain. In other words,
229 initial HDL-binding and subsequent occupation of the active site by a ligand are most likely
230 responsible for triggering the lid opening and rearrangement of the cap domain we observe in the
231 structure, and not the binding of **1**.
232
233 As these conformational changes in the lid and reorientation of the cap domain occur, there are
234 resulting alterations within the active site that facilitate binding to substrates. In LPLA2, two
235 distinct tracks for the acyl chains of lipid substrates were observed (Figure S3c) (Glukhova et al.,
236 2015). Track A is furthest from the lid loop and is only solvent-accessible when the lid is

237 retracted, and the α5 helix, including hinge residue Trp251, unwinds and moves inwards to block
238 this track in the closed lid conformation of LCAT-closed (Figure S5). In the lid-open structures,
239 Lys218 moves with the cap domain away from the MBD in the activated conformation, where it
240 would be in better position to bind the phosphate in the substrate lipid head group(Glukhova et
241 al., 2015) (Figure S5a).
242
243 **Structure-activity relationships**
244 The structure of the ΔNΔC-IDFP·**1** complex confirms the structure-activity relationships we and
245 others have observed for the pyrazolopyridine scaffold. The hydrogen bonds formed by the
246 pyrazole ring with the backbone carbonyl of Met49 and amide of Tyr51 (Figure 2b-c) indicate
247 that **1-b** is the dominant tautomerized isoform in the co-crystallized structure (Figure S2a).
248 Although the exchange of pyrazole (**2**) to imidazole (**3**) eliminates the hydrogen bond with
249 Met49, this resulted in only a minimal change in EC_{50} (280 and 320 nM for **2** and **3**,
250 respectively) and no change in the maximum response (Table 1, 2). However, interruption of
251 both of these hydrogen bonds by swapping the pyrazole (**2**) for isoxazole (**9**, Figure S2b)
252 dramatically increased the EC_{50} to 7.7 μM and decreased the response to 1.6-fold (Table 2, 5). It
253 was previously shown that removal of the C4 hydroxyl group (**4**, Figure S2b), which interacts
254 with Asp63 in the structure, caused a ~6-fold drop in potency compared with **2** (Kobayashi et al.,
255 2015a; Kobayashi et al., 2015b). This is consistent with elimination of the hydroxyl group of **3** to
256 give the more planar structure of **8** (Figure S2b) which decreased the potency to 4.6 μM, yet
257 interestingly it activated LCAT with increased efficacy of 3.7-fold (Table 2, 5). Surprisingly,
258 although the bicyclic head of these compounds is expected to play an important role in the
259 retention of potency, the imidazole-containing head group of **3** has no activating effect at

concentrations up to 10 μM (**6**, Figure S2b), perhaps due to loss of favorable interactions with Met49. Consistent with the above data, compounds **6**, **8**, and **9** could not thermal stabilize LCAT at 10 μM in DSF, although **8** could at 100 μM (Figure S6a). MST further confirmed that **6** was unable to bind to LCAT (Figure S6b). Thus, in this series of activators, potency and efficacy are therefore highly dependent on a hydroxyl and chirality at the C4 position, as well as maintenance of a pyrazine ring system that likely assists in interactions with hydrophobic substrates.

Perturbation of the activator binding site

To further validate the crystal structure and better understand the mechanistic role of the MBD, we exchanged residues in the activator binding site of LCAT with their equivalents in LPLA2, which is not stabilized by **1** or related compounds (Figure 1g). The Y51S, G71I, and Y51S/G71I (Figure 3a) variants were thus expected to be impaired in binding. These variants exhibited similar or higher T_m values than WT LCAT, and were able to hydrolyze both the soluble substrate *p*-nitrophenyl butyrate (pNPB) and the micellar substrate MUP (Figure 4, S7), indicating an intact fold. As expected, **1** was far less effective at increasing the T_m of the three variants compared to WT (Figure 4a). The Y51S/G71I variant also exhibited a nearly 4-fold decrease in HDL binding affinity and a reduced ability to catalyze acyl transfer (Figure 4b-c, S8). These results are consistent with recent studies probing nearby positions at Trp48 (mutated to Ala) and Leu70 (mutated to Ser) (Manthei et al., 2017) or the analogous positions in LPLA2 (Glukhova et al., 2015). Conversely, the analogous LPLA2 chimeric variants (S33Y, I53G, and S43Y/I53G) had lower T_m values relative to WT (Figure 4a). However, these variants remained unable to be stabilized by **1**. We were unable to express and test a triple mutant expected to fully restore binding (S33Y/I53G/L48N).

Compound **1** did not stimulate pNPB esterase activity for any variant of LCAT (Figure S7b), and in fact seemed to inhibit the activity of WT. Perturbation of the activator binding site decreased this effect. Compound **1** and related compounds activated hydrolysis in the MUP assay (Figure 4d, Table 1, 2). The EC_{50} of Y51S with **1** was 4-fold higher than WT at 0.59 μM, G71I had an EC_{50} > 5 μM, and Y51S/G71I had no response at concentrations up to 10 μM **1**. We confirmed these results in a DHE acyltransferase assay with the Y51S/G71I variant, wherein the mutation failed to increase activity in the presence of compound **2** (Figure 4c, e, Table 1). These results confirm that the binding site for **1** in the crystal structure is responsible for the biochemical effects observed in solution.

Recovery of activity in an FLD variant

Arg244 is a position commonly mutated in LCAT genetic disease (R244G (McLean, 1992; Vrabec et al., 1988), R244H (Pisciotta et al., 2005; Sampaio et al., 2017; Strom et al., 2011), R244C (Charlton-Menys et al., 2007), and R244L (Castro-Ferreira et al., 2018)) and its side chain forms unique interactions in the observed active and inactive states of LCAT. In data obtained from patient plasma, the amount of LCAT-R244G isolated from homozygotes was ~25% of the amount from WT LCAT plasma and there was ~15% of WT LCAT activity, whereas heterozygotes of the R244G and R244H mutations had ~80% and ~50% of WT LCAT activity, respectively (Pisciotta et al., 2005; Vrabec et al., 1988), thus supporting an important role for this residue. Arg244 is found in the lid of LCAT and interacts with the backbone carbonyls of Leu223 and Leu285 in ΔNΔC-IDFP·**1**, and with the side chain of Asp335 in the lid closed state of LCAT-closed (Figure 5a, Movie S1). We hypothesized that molecules targeting the MBD could restore some stability and function of mutations at Arg244 because this residue does not participate in

306 the binding site for **1**. The LCAT-R244A and -R244H variants were purified and shown to be
307 less stable than WT with ΔT_m values of -2.3 and -2.4 ˚C, respectively, consistent with Arg244
308 playing an important structural role (Figure 5b, S7a). Both LCAT-R244A and -R244H exhibited
309 WT levels of pNPB activity, but 44% and 78% of WT in the MUP hydrolysis assay (Figure S7b-
310 c). In HDL binding analyses, both variants had an increased k_{off} (2-fold for R244A and 3.5-fold
311 for R244H) which led to an increase in their overall K_d values (Figure S8, Table 3). For R244H,
312 the k_{on} was also decreased from 0.091 (WT) to 0.022 μM^{-1} s^{-1}. Thus, in the context of HDL
313 binding, the histidine mutant is less tolerated, perhaps due to steric clashes in the lid open
314 conformation. Neither variant had substantial activity in the acyltransferase assay (Figure 5c),
315 consistent with their contribution to FLD.
316
317 R244A and R244H were both stabilized by the addition of compound **1** (ΔT_m of 6.0 and 4.8 ˚C,
318 respectively, Figure 5b). R244A, R244H, and WT LCAT all exhibited similar EC_{50} values in
319 response to **1** in the MUP esterase assay (~150 nM), with all three variants being activated about
320 2-fold by compounds **1**-**3** (Figure 5d, Table 1, 2). In the DHE acyltransferase assay, the EC_{50}
321 values in the presence of saturating **2** were 0.28, 0.76, and ≥ 4.6 μM for WT, R244A, and
322 R244H, respectively (Figure 5e, Table 1). At the highest concentration tested (10 μM compound
323 **2**), the acyltransferase rate was 18 and 26 μM h^{-1} for R244A and R244H, respectively, both
324 greater than WT LCAT which had a rate of 11 μM h^{-1} at the lowest concentration of **2** examined.
325 The activator affected HDL binding of the two Arg244 variants differently. For R244A,
326 compound **1** decreased the k_{on} from 0.069 to 0.017 μM^{-1} s^{-1}, which increases the K_d from 3.2 to
327 11 μM. For R244H, compound **1** enhanced binding to HDL by reducing the k_{off} from 0.40 to 0.15
328 s^{-1}, reducing the K_d from 18 to 4.3 μM (Figure S8, Table 3). Thus, piperidinylpyrazolopyridine

329 and piperidinylimidazopyridine activators like **1** can partially rescue defects in activity for
330 LCAT-Arg244 variants.
331
332 **DISCUSSION**
333 Here we have defined a novel activator binding site in the MBD of LCAT as well as the active
334 conformation of LCAT, and have demonstrated that these activators can restore the activity of
335 some FLD variants. However, the mechanism of activation mediated by **1** and its analogs is not
336 straightforward. The activators do not alter the binding constant of WT LCAT for HDL (Figure
337 1e, Table 3), suggesting that they do not contribute to HDL binding despite occupying a site in
338 the MBD. Thus, one would expect that the residues that interact with **1** would not be involved in
339 HDL binding, or else these compounds would act as inhibitors. However, the site is closely
340 juxtaposed with residues that are definitely involved in HDL binding. Important HDL-binding
341 residues such as Trp48 and Leu70 are adjacent to the activator binding site (Manthei et al.,
342 2017), and the double mutant Y51S/G71I was 4-fold decreased in its affinity for HDLs due to a
343 defect in the k_{off}, and lost acyltransferase activity (Figure 4, Table 3). A G71R variant has also
344 been reported in LCAT genetic disease (Hörl et al., 2006).
345
346 The compounds increase activity of WT LCAT up to 3.7-fold, specifically by increasing the
347 V_{max}, although remote from the catalytic triad and IDFP binding site (Figure 1, Table 2). The
348 typical mechanism for acting at a distance would be allostery, wherein ligand binding induces a
349 conformational change that alters the active site. Indeed, ΔNΔC-IDFP·**1** adopts what we believe
350 is a more active state with alterations in the active site that should promote activity. However, the
351 MBD of LCAT does not appreciably change its orientation with respect to the hydrolase domain

in any reported structure thus far, and the activator binding site seems available regardless of LCAT conformation. Moreover, the increase in T_m caused by IDFP and compound **1** is additive, not synergistic (Figure 1f-g), and our previous HDX MS data suggested that IDFP alone can stabilize LCAT in an active, lid open conformation that is likely represented by the current structure (Manthei et al., 2017). Thus, IDFP is more likely to be the driver of the observed global conformation change observed in the crystal structure of ΔNΔC-IDFP·**1**. Although both ligands stabilize, they do so via independent mechanisms and **1** may only do so locally.

Thus, we hypothesize that the activators such as **1** act by stabilizing the MBD and facilitating substrate entry into the active site cleft of the enzyme. In support of such a model, we note that the two chains of LCAT in the asymmetric unit of the ΔNΔC-IDFP·**1** crystals pack to form a pseudo-symmetric homodimer utilizing an interface with many of the hydrophobic residues from the MBD including Trp48, Leu64, Phe67, Leu68, Pro69, Leu70 and Leu117 from the αA-αA′ loop (Figure S3a, S9). The interface is centered on the side chains of Leu64 and Phe67. The pyrazine ring of the activator is prominently featured in this hydrophobic surface. This hydrophobic ring packs next to residues in the MBD well-known to be important for membrane interactions, such as the conspicuously solvent exposed Trp48 side chain (Figure S9a). This same interface was also proposed by a recent molecular dynamics study exploring the ability of LCAT to dock to a model membrane in both the closed and open conformations (Casteleijn et al., 2018). In the closed conformation, the active site lid blocks Leu64, Phe67, and Leu117 from being able to access membranes, though the rest of the MBD and the hydrophobic N-terminus of LCAT, which is also key for HDL binding (Manthei et al., 2017), would still be available (Figure S9b). The simulations in this study also suggested that residues such as Phe67 were involved in

promoting transfer of lipids into the active site tunnel of the enzyme. Mutation of Arg244, unlike compound **1**, clearly affects binding to HDL, and thus this residue, or the lid region in which it resides, could be a major ApoA-I binding determinant (Figure S8, Table 3). Indeed, a recent paper identified a crosslink between LCAT and ApoA-I at nearby residue Lys240 within the lid (Cooke et al., 2018).

A better understanding of how ligands fit within the activator pocket enables rational design to create more potent and effective LCAT activators. For example, our crystal structure revealed the preferred enantiomer of bound piperidinylpyrazolopyridines, thus one could expect at least two-fold higher potency could be achieved with an enantiopure preparation. A recent patent has improved the potency of these compounds 3-fold by using an optically pure compound, as well as adding a hydroxyl to the C5 position on the bicyclic head, which our structure indicates would add a second hydrogen bond with the side chain of Asp63 (Kobayashi et al., 2016). Furthermore, we have shown that there is potential to increase the efficacy of the compounds, as **8** activated 3.7-fold as compared to the parent compounds activating an average of 2.3-fold. However, **8** had lowered potency, and so more modulations will be required to determine if potency and efficacy can be improved simultaneously.

The ability to perform rational design is important because we also demonstrated here the therapeutic potential of using small molecule activators targeting the MBD in FLD patients. We focused on mutations at Arg244 (Castro-Ferreira et al., 2018; Charlton-Menys et al., 2007; McLean, 1992; Pisciotta et al., 2005; Sampaio et al., 2017; Strom et al., 2011; Vrabec et al., 1988) because of its apparent role in the switch mechanism of the active site lid, but in principle

any patient harboring an alternative missense mutation that does not directly perturb the hydrolase active site may also benefit from this compound series. Even a relatively small increase in activity could potentially slow or reverse the progression of renal disease in some FLD patients because FED patients with only partial LCAT activity do not develop renal disease (Ahsan et al., 2014). Certainly, treatment with a small molecule activator would be more cost effective and easier for patients comply with than rhLCAT enzyme replacement therapy. In future experiments, it will be important to examine the utility of activators like **1** for other FLD variants. Lastly, because these compounds were demonstrated to effectively increase HDL-C in monkeys with normal levels of LCAT (Kobayashi et al., 2016; Kobayashi et al., 2015a; Kobayashi et al., 2015b; Onoda et al., 2015), it will be important to continue to interrogate their mechanism and determine if they also increase cholesterol efflux and promote atherosclerotic plaque regression. If so, then activation of LCAT by a small molecule approach and improving HDL function could be widely used in the primary prevention of cardiovascular disease and would likely complement our existing drugs for lowering LDL-C, such as statins and PCSK9-inhibitors.

MATERIALS AND METHODS

Cell Culture, Protein Production, and Purification

To produce protein for crystallographic screens, a stable cell line expressing ΔNΔC-LCAT was created in HEK293F cells. A codon-optimized human ΔNΔC-LCAT construct with a C-terminal 6x histidine-tag in pcDNA4 was SspI digested and transfected into HEK293F cells (Invitrogen). Cells were selected with zeocin and grown in adherent culture on 150 mm plates in Dulbecco's Modified Eagle Medium high glucose medium with GlutaMAX and 1 mM pyruvate

(ThermoFisher), supplemented with 10% fetal bovine serum (Sigma), 100 U/ml penicillin, 100 µg/ml streptomycin and 50 µg mL^{-1} zeocin. Kifunensine (Cayman Chemical) was added to 5 µM once the cells were confluent to prevent complex glycosylation. Conditioned media was harvested every 5 days, purified via Ni-NTA, dialyzed against reaction buffer (20 mM HEPES pH 7.5, 150 mM NaCl), and then frozen. For crystallographic trials, samples were thawed and subsequently cleaved with a 1:3 endoglycosidase H:LCAT molar ratio in reaction buffer supplemented with 100 mM NaOAc pH 5.2 for 2.5 h at room temperature, which reduces the heterogeneous *N*-glycans to single *N*-acetylglucosamines. HEPES pH 8 was then added to 100 mM prior to re-purification via Ni-NTA to remove the glycosidase, and finally LCAT was polished via tandem Superdex 75 size exclusion chromatography (SEC) in reaction buffer (20 mM HEPES pH 7.5, 150 mM NaCl).

Protein for biochemical analysis was made using pcDNA4 containing the codon-optimized human LCAT gene with a C-terminal 6x histidine-tag, which was transiently transfected in HEK293F (Invitrogen) cells as previously described (Glukhova et al., 2015). The cells were grown in suspension in FreeStyle (ThermoFisher) medium supplemented with 100 U mL^{-1} penicillin and 100 µg mL^{-1} streptomycin, and conditioned media was harvested 5 d later. The secreted protein was purified via Ni-NTA and dialyzed against reaction buffer. The LCAT proteins used in pNPB, MUP, and DSF experiments were further polished via Superdex 75 SEC to remove any background contaminating reactivity.

444 **Crystallization and Structure Determination**

445 ΔNΔC-LCAT was derivatized with isopropyl dodecyl fluorophosphonate (IDFP, Cayman
446 Chemical) to give ΔNΔC-IDFP in reaction buffer as previously described (Manthei et al., 2017).
447 ΔNΔC-IDFP at 5 mg mL^{-1} was incubated with 1 mM compound **1** for 30 min at room
448 temperature in reaction buffer with 1% DMSO. Sparse matrix screens were set with a Crystal
449 Gryphon (Art Robbins Instruments). Initial crystals of ΔNΔC-IDFP·**1** were obtained via sitting
450 drop vapor diffusion from the Index HT screen (Hampton). Crystals formed at 20 ˚C in a 1 µL
451 drop with a protein to mother liquor ratio of 1:1. The crystals were optimized to a final condition
452 of 0.25 M lithium sulfate, 0.1 M Tris pH 8.5, and 16% PEG 3350 via hanging drop vapor
453 diffusion, and cryoprotected by moving the crystals to buffer with 0.2 M lithium sulfate, 0.1 M
454 Tris pH 8.5, and 24% PEG 3350, and 20% glycerol. Crystals were frozen in nylon cryoloops
455 (Hampton), and the data were collected at the Advanced Photon Source (APS) at Argonne
456 National Laboratories on the LS-CAT 21-ID-G (λ=0.97857) beam line. The data were processed
457 and scaled with HKL2000 (Otwinowski and Minor, 1997). The closed LCAT structure (PDB
458 5TXF) with the lid removed (residues 226-249) was used as a search model in molecular
459 replacement with PHASER (McCoy et al., 2007) to generate initial phases. Non-crystallographic
460 symmetry (NCS) restraints were applied to the two copies of LCAT per asymmetric unit during
461 refinement in REFMAC5 (Murshudov et al., 2011) and Phenix (Adams et al., 2010) but removed
462 during the final rounds of refinement. Reciprocal space refinement alternated with manual model
463 building in Coot (Emsley et al., 2010). A Ni^{2+} was observed coordinated by a portion of the
464 exogenous His-tag beginning at residue 398 of chain A and aided in crystal packing. The final
465 model was validated for stereochemical correctness with MolProbity (Chen et al., 2010).
466

467 **Soluble Esterase Assay**

468 The esterase assay was performed as previously described (Glukhova et al., 2015) at least in
469 triplicate. pNPB (Sigma-Aldrich) was diluted to 10 mM into reaction buffer containing 10%
470 dimethylsulfoxide. The reaction was started by addition of 40 µL 1 µM LCAT containing either
471 3.2 % DMSO or 11.1 µM compound **1** to 10 µL of pNPB. The increase in absorbance at 400 nm
472 was monitored on a Spectramax plate reader for 15 min. Significance was determined using a
473 one-way analysis of variance followed by Tukey's multiple comparisons post-test in GraphPad
474 Prism.

475

476 **MUP Hydrolysis Assay**

477 The lipase activity of LCAT was measured using MUP as a substrate. The assay was performed
478 at room temperature in 0.1 M sodium phosphate buffer, pH 7.4 containing 0.01% Triton X-100. 4
479 µL of LCAT (6 nM final concentration) were dispensed into a 1536-well Greiner solid black
480 plate. The same volume of assay buffer was dispensed into column 1 and 2 for a no-enzyme
481 control. Then 23 nL DMSO or compounds titrated at 11-point 1:3 dilution series starting at 10
482 mM were transferred using a pintool. After 15 min incubation, 2 µL MUP (16 µM final
483 concentration) was added to initiate the reaction. The hydrolysis of MUP was monitored using a
484 ViewLux plate reader (excitation 380 nm/emission 450nm) for 20 min. The fluorescence signal
485 was normalized against no-activator and no-enzyme control after subtraction of background
486 signal (t=0 min). To plot percent activation, in each assay 100% was set at the rate of LCAT or
487 LCAT variant without compound. The resulting data were fitted to a sigmoidal dose response
488 curve.

489

490 **Differential Scanning Fluorimetry**

491 T_m values were determined using an Applied Biosystems QuantStudio 7 Flex qPCR machine
492 with two replicates performed at least in triplicate. LCAT at 0.05 mg mL^{-1} was diluted into
493 reaction buffer containing 5X Sypro Orange (Invitrogen) in a final volume of 10 µL in 384-well
494 PCR plates. DMSO or compound **1** was added so that all reactions contained 3% DMSO. The
495 reactions were run from 25-95 ˚C with a ramp rate of 0.03 ˚C s^{-1}. T_m values were determined as
496 the derivative using Protein Thermal Shift software. Significance was determined using a one-
497 way analysis of variance followed by Tukey's multiple comparisons post-test in GraphPad Prism.
498

499 **MST Binding Assay**

500 MST was used to determine the binding affinity of the compounds to LCAT. Recombinant
501 proteins were labeled with a fluorophore using the Monolith His-tag labeling RED-Tris-NTA
502 2nd Generation kit (Nanotemper Technologies) following manufacturer's protocol. Compounds
503 were titrated in a two-fold dilution series starting at 20 µM and incubated with the same volume
504 of 100 nM labeled recombinant protein for 5 min at room temperature. Measurements were
505 carried out in PBS containing 0.05% Tween-20 and standard capillaries using a Monolith
506 NT.115 instrument (Nanotemper Technologies) with 50% LED excitation power, 60% MST
507 power, MST on-time of 30 s and off-time of 5 s. K_d values were calculated by fitting the
508 thermophoresis signal at 20 s of the thermograph using MO.AffinityAnalysis software
509 (Nanotemper Technologies).
510
511
512

513 **Bio-Layer Interferometry**

514 A FortéBio Octet RED system was used to measure the binding of LCAT to ApoA-I HDLs.
515 HDLs were prepared with 1,2-dipalmitoyl-sn-glycero-3-phosphocholine (DPPC, Avanti), 1-
516 palmitoyl-2-oleoyl-sn-glycero-3-phosphocholine (POPC, NOF America), and 16:0 biotinyl Cap
517 PE (Avanti) in a ratio of 49.5:49.5:1 (Manthei et al., 2017). HDLs were diluted 1/20 in assay
518 buffer (1X PBS pH 7.4, 1 mM EDTA, 60 μM fatty acid free bovine serum albumin (Sigma-
519 Aldrich)) and then immobilized on streptavidin tips for 600 s, followed by a wash in assay buffer
520 for 600 s to remove unbound HDLs. The tips were then moved to buffer containing DMSO or
521 compound **1** and allowed to equilibrate for 120 s before a baseline was established for 30 s. The
522 tips were then moved into LCAT protein in assay buffer (containing DMSO or 10 μM **1**) or
523 buffer alone (with DMSO or 10 μM **1**) as a control and allowed to associate for 200 s, and then
524 dissociated in assay buffer for 480 s. All steps were performed at 25 ˚C with shaking at 1000
525 rpm. LCAT was titrated from 0.4 – 2.4 μM in triplicate. However, for some data sets (R244H,
526 R244H + **1**, and Y51S/G71I), the 0.4 μM point was excluded due to low signal. The appropriate
527 control of buffer containing DMSO or **1** was used to subtract the baseline and correct for drift
528 using FortéBio's Data Analysis 7.0. The association and dissociation curves were fit using
529 GraphPad Prism with a two-phase model. In order to determine K_d values, the k_{obs} (from
530 association) were determined at each concentration for the fast phase and then plotted against
531 LCAT concentration. The slope of the line was evaluated as k_{on} using the equation $k_{obs} =$
532 $k_{on}[LCAT] + k_{off}$ and the resultant $K_d = k_{off}/k_{on}$. For statistical analysis, the k_{on}, k_{off}, and K_d for
533 each replicate was determined individually and the results were compared to WT using a one-
534 way analysis of variance followed by Tukey's multiple comparisons post-test in GraphPad Prism.
535

DHE Acyltransferase Assay

Peptide-based HDLs were used in this assay as there is no difference between peptide HDLs and ApoA-I HDLs in both HDL binding and acyltransferase assays (Manthei et al., 2017). The peptide HDLs were made using the ESP24218 peptide with the sequence PVLDLFRELLNELLEALKQKLK (Dassuex et al., 1999; Li et al., 2015) with a DPPC:POPC:DHE ratio of 47:47:6 as previously described (Manthei et al., 2017). The assay was performed in 384-well low volume black microplates (Corning 4514) with a total assay volume of 16 µL. In each reaction, LCAT was diluted in assay buffer to 15 µg mL^{-1} in the presence of either 1% DMSO or 10 µM **2** with 1% DMSO. **2** was used in this assay because it has lower background fluorescence than **1**. The DHE HDLs were diluted in 1X PBS with 1 mM EDTA and 5 mM β-mercaptoethanol. 8 µL of the HDLs were added to the plate, and the reactions were initiated with 8 µL of LCAT, so that LCAT was assayed at 7.5 µg mL^{-1} with and without 5 µM compound with a range of DHE concentrations from 0 – 50 µM. The reactions were stopped after 25 min at 37 ˚C with the addition of 4 µL of stop solution (1X PBS with 1 mM EDTA, 5 U mL^{-1} cholesterol oxidase (COx), and 7% Triton X100). Following the addition of stop solution, the plates were incubated for another 60 min at 37 ˚C to allow for the COx to react. After the plates were re-equilibrated at room temperature, fluorescence was determined on a SpectraMax plate reader with excitation at 325 nm and emission at 425 nm, with a 420 nm cutoff. Reactions without LCAT were used for background subtraction, and reactions without LCAT and stop solution lacking COx were used to generate a standard curve for DHE. Reactions were performed in triplicate with three independent experiments per LCAT variant. Data were processed via background subtraction to remove excess fluorescence that results from the higher concentrations of DHE. These values were divided by the slope of the line from the standard

559 curve, which yields the amount of DHE-ester that resulted in each well, and then by time to
560 determine the rate. Outliers were removed using automatic outlier elimination within Prism. For
561 statistical analysis, the V_{max} for each variant was compared to WT using a one-way analysis of
562 variance followed by Tukey's multiple comparisons post-test in GraphPad Prism.
563
564 To determine EC_{50} values, **2** was titrated from 0.004–10 μM, and the DHE concentration was set
565 at 50 μM. LCAT was diluted in assay buffer and compound **2** dilutions were made with assay
566 buffer containing 5.3% DMSO. 1.5 μL compound was added, then 6.5 μL LCAT, followed by 8
567 μL DHE. Dilutions were adjusted so that LCAT was assayed at 7.5 μg mL^{-1}, as above. All values
568 were background subtracted to buffer with the same concentration of **2**. A standard curve was
569 included in one experiment with DHE from 0–50 μM in order to adjust the final fluorescence
570 values to a rate by dividing by the slope of the line and time (25 min), as above. Outliers were
571 removed using automatic outlier elimination within Prism. For statistical analysis, the EC_{50} for
572 each variant was compared to WT using a one-way analysis of variance followed by Tukey's
573 multiple comparisons post-test in GraphPad Prism.
574
575 **Statistical Analysis**
576 In most cases and as indicated in the methods and figure legends, statistical analysis was
577 performed a one-way analysis of variance followed by Tukey's multiple comparisons post-test in
578 GraphPad Prism. A paired t-test was used to compare the basal MUP hydrolysis levels. The
579 statistical parameters, P value cutoffs, and number of replicates for each experiment are indicated
580 in the table that corresponds to each experiment, the figure legends, and/or methods.
581

582 **CHEMICAL SYNTHESIS**

583 **General Methods for Chemistry**

584 All air or moisture sensitive reactions were performed under positive pressure of nitrogen with
585 oven-dried glassware. Chemical reagents and anhydrous solvents were obtained from
586 commercial sources and used as is. Preparative purification was performed on a Waters semi-
587 preparative HPLC. The column used was a Phenomenex Luna C18 (5 micron, 30 x 75 mm) at a
588 flow rate of 45 mL min^{-1}. The mobile phase consisted of acetonitrile and water (each containing
589 0.1% trifluoroacetic acid). A gradient of 10% to 50% acetonitrile over 8 min was used during the
590 purification. Fraction collection was triggered by UV detection (220 nm). Analytical analysis for
591 purity was determined by two different methods denoted as Final QC Methods 1 and 2. Method
592 1: analysis was performed on an Agilent 1290 Infinity Series HPLC with a 3 min gradient from
593 4% to 100% acetonitrile (containing 0.05% trifluoroacetic acid) followed by 1.5 min at 100%
594 acetonitrile with a flow rate of 0.8 mL min^{-1}. A Phenomenex Luna C18 column (3 micron, 3 x 75
595 mm) was used at a temperature of 50 °C. Method 2: analysis was performed on an Agilent 1260
596 with a 7 min gradient of 4% to 100% acetonitrile (containing 0.025% trifluoroacetic acid) in
597 water (containing 0.05% trifluoroacetic acid) over 8 min run time at a flow rate of 1 mL min^{-1}. A
598 Phenomenex Luna C18 column (3 micron, 3 x 75 mm) was used at a temperature of 50 °C.
599 Purity determination was performed using an Agilent Diode Array Detector for both Method 1
600 and Method 2. Mass determination was performed using an Agilent 6130 mass spectrometer with
601 electrospray ionization in the positive mode. All of the analogs for assay have purity greater than
602 95% based on both analytical methods. ^{1}H NMR spectra were recorded on Varian 400 MHz
603 spectrometers.
604

The LCAT activators were synthesized as shown in the scheme in Figure 6.

Synthesis of 4-Hydroxy-3-(piperidin-4-yl)-4-(trifluoromethyl)-4,5-dihydro-1H-pyrazolo[3,4-*b*]pyridin-6(7H)-one, HCl (5)

Step 1: To a solution of tert-butyl 4-(5-amino-1H-pyrazol-3-yl)piperidine-1-carboxylate (**5a**, 799 mg, 3 mmol) in acetic acid (9 ml) was added ethyl 4,4,4-trifluoro-3-oxobutanoate (1657 mg, 9.0 mmol). The mixture was then heated at 60 °C for 3 h. After cooling to room temperature (RT), the mixture was diluted with EtOAc (20 mL) and was added saturated $NaHCO_{3(aq)}$ slowly until the pH of aqueous layer is ~ 7. The solution was extracted with EtOAc (50 mL x 3). The combined organic layer was dried (Na_2SO_4) and filtered. After removal of solvent, the product was purified by silica gel chromatography using 0-5% MeOH/EtOAc as the eluent to give tert-butyl 4-(4-hydroxy-6-oxo-4-(trifluoromethyl)-4,5,6,7-tetrahydro-1H-pyrazolo[3,4-b]pyridin-3-yl)piperidine-1-carboxylate (**5b**, 690 mg, 1.71 mmol, 56.9 % yield).

Step 2: To a solution of tert-butyl 4-(4-hydroxy-6-oxo-4-(trifluoromethyl)-4,5,6,7-tetrahydro-1H-pyrazolo[3,4-b]pyridin-3-yl)piperidine-1-carboxylate (**5b**, 690 mg, 1.71 mmol) in 1,4-dioxane (4 ml) was added HCl (4M in dioxane, 2.6 mL, 10.2 mmol, 6 equiv) at 0 °C. The mixture was then stirred at RT for 2 h. Then, hexane (15 mL) was added. The solid was filtered, washed with hexane (3 mL x 2), and then dried in vacuo to give 4-hydroxy-3-(piperidin-4-yl)-4-(trifluoromethyl)-4,5-dihydro-1H-pyrazolo[3,4-b]pyridin-6(7H)-one, HCl (**5**, 559 mg, 1.64 mmol, 96%). The material was used without further purification. LC-MS (Method 1): t_R = 2.14 min, m/z $(M+H)^+$ = 305.

628 **Synthesis of 7-Hydroxy-1-(piperidin-4-yl)-7-(trifluoromethyl)-6,7-dihydro-1H-imidazo[4,5-**
629 **b]pyridin-5(4H)-one, HCl (6)**

630 Step 1: To a mixture of 4-nitro-1H-imidazole (**6a**, 3.39 g, 30.0 mmol) and K_2CO_3 (4.2 g, 30.0
631 mmol) was added DMF (40 ml). The mixture was stirred at 110 °C for 1 h and tert-butyl 4-
632 ((methylsulfonyl)oxy)piperidine-1-carboxylate (5.6 g, 20 mmol) was added and stirred at 110 °C
633 for overnight. The mixture was poured into EtOAc (200 mL)/H_2O (200 mL). The aqueous layer
634 was extracted with EtOAc (150 mL x 2). The combined organic layer was concentrated to ~ 200
635 ml of solvent left. The organic solution was washed with H_2O (200 mL x 2), dried (Na_2SO_4) and
636 filtered. After removal of solvent, some solid (nitroimidazole) from crude mixture can be filtered
637 out by trituration with 50% EtOAc/hexane. The filtrate was concentrated and purified by silica
638 gel chromatography using 30-70-100% EtOAc/hexane as the eluent to give tert-butyl 4-(4-nitro-
639 1H-imidazol-1-yl)piperidine-1-carboxylate (**6b**, 2.25 g, 7.59 mmol, 38.0 % yield).
640
641 Step 2: In a 2-neck flask was placed tert-butyl 4-(4-nitro-1H-imidazol-1-yl)piperidine-1-
642 carboxylate (**6b**, 2.4 g, 8 mmol) and Pd-C (0.43 g, 0.40 mmol). Then, EtOH (50 ml) was added.
643 The air was removed by house vacuum and refilled with N_2 for 2 times. Then, a H_2 balloon was
644 attached. The N_2 air was removed by house vacuum and refilled with H_2 for 3 times. The mixture
645 was stirred at RT for 2.5 h. The H_2 balloon was removed and refilled with N_2. The mixture was
646 filtered to remove most of Pd and the filtrate was then filtered again through a nylon 0.45 μM
647 filter using EtOH as the eluent. The filtrate was concentrated to move most of EtOH until ~ 2-3
648 mL left. Then, to the crude product was added EtOH (6 mL), acetic acid (12 ml), and then ethyl
649 4,4,4-trifluoro-3-oxobutanoate (3.51 ml, 24.0 mmol). The mixture was then stirred at 65-70 °C
650 for 2.5 h. After cooling to RT, the mixture was diluted with EtOAc (50 mL)/H_2O (30 mL) and

651 was added saturated $NaHCO_{3(aq)}$ slowly until the pH of aqueous layer is ~ 7. The solution was
652 extracted with EtOAc (70 mL x 3). The combined organic layer was dried (Na_2SO_4) and filtered.
653 After removal of solvent, the product was purified by silica gel chromatography using 0-5-10%
654 MeOH/EtOAc as the eluent to give tert-butyl 4-(7-hydroxy-5-oxo-7-(trifluoromethyl)-4,5,6,7-
655 tetrahydro-1H-imidazo[4,5-b]pyridin-1-yl)piperidine-1-carboxylate (**6c**, 2.78 g, 6.87 mmol, 86 %
656 yield). LC-MS (Method 1): t_R = 2.14 min, m/z $(M+H)^+$ = 405.
657
658 Step 3: To a solution of tert-butyl 4-(7-hydroxy-5-oxo-7-(trifluoromethyl)-4,5,6,7-tetrahydro-1H-
659 imidazo[4,5-b]pyridin-1-yl)piperidine-1-carboxylate (**6c**, 222 mg, 0.549 mmol) in 1,4-dioxane (2
660 ml) was added HCl (4M in dioxane, 1.1 mL, 4.39 mmol, 8 equiv) at 0 °C. The mixture was then
661 stirred at RT for 2 h. Then, hexane (15 mL) was added, stirred, and then the hexane solvent was
662 carefully removed (3 times). The solid was then dried in vacuo to give 7-hydroxy-1-(piperidin-4-
663 yl)-7-(trifluoromethyl)-6,7-dihydro-1H-imidazo[4,5-b]pyridin-5(4H)-one, HCl (**6**, 180 mg, 0.528
664 mmol, 96 % yield). The material was used without further purification. LC-MS (Method 1): t_R =
665 2.07 min, m/z $(M+H)^+$ = 305.
666
667 **Synthesis of 4-Hydroxy-3-(piperidin-4-yl)-4-(trifluoromethyl)-4,5-dihydroisoxazolo[5,4-**
668 **b]pyridin-6(7H)-one, HCl (7)**
669 Step 1: To a mixture of tert-butyl 4-(2-cyanoacetyl)piperidine-1-carboxylate (**7a**, 2.02 g, 8
670 mmol) and hydroxylamine, HCl (0.70 g, 10.0 mmol) in CH_2Cl_2 (20 ml) was added Et_3N (2.23
671 ml, 16.0 mmol). The mixture was sealed and stirred at 55 °C for overnight. After cooling to RT,
672 the mixture was poured into CH_2Cl_2/H_2O (30 mL/30 mL). The aqueous layer was extracted with
673 CH_2Cl_2 (30 mL). The combined organic layer was dried (Na_2SO_4) and filtered. After removal of

674 solvent, the product was purified by silica gel chromatography using 60-100% EtOAc/hexane as
675 the eluent to give tert-butyl 4-(5-aminoisoxazol-3-yl)piperidine-1-carboxylate (**7b**, 1.89 g, 7.08
676 mmol, 88 % yield) ^{1}H NMR (400 MHz, DMSO-d_6) δ 6.47 (s, 2H), 4.81 (s, 1H), 3.91 (d, J = 13.1
677 Hz, 2H), 2.79 br (s, 2H), 2.61 (tt, J = 11.5, 3.7 Hz, 1H), 1.80 - 1.69 (m, 2H), 1.43-1.33 (m, 11H);
678 LC-MS (Method 1): t_R = 3.05 min, m/z $(M+Na)^+$ = 290.
679
680 Step 2: To a solution of tert-butyl 4-(5-aminoisoxazol-3-yl)piperidine-1-carboxylate (**7b**, 535
681 mg, 2 mmol) in EtOH (2 ml) and AcOH (4 ml) was added ethyl 4,4,4-trifluoro-3-oxobutanoate
682 (1105 mg, 6.0 mmol). The tube was sealed and heated at 70 °C for 6 h. The mixture was diluted
683 with EtOAc/H_2O (10 mL/10 ml). Then, saturated $NaHCO_{3(aq)}$ was added dropwise to the stirring
684 mixture until the pH of aqueous layer was ~ 7. The aqueous layer was extracted with EtOAc (30
685 mL x 2). The combined organic layer was dried (Na_2SO_4) and filtered. After removal of solvent,
686 the product was purified by silica gel chromatography using 20-70% EtOAc/hexane as the eluent
687 to give tert-butyl 4-(4-hydroxy-6-oxo-4-(trifluoromethyl)-4,5,6,7-tetrahydroisoxazolo[5,4-
688 b]pyridin-3-yl)piperidine-1-carboxylate (**7c**, 520 mg, 1.28 mmol, 64.1 % yield). ^{1}H NMR (400
689 MHz, DMSO-d_6) δ 11.96 (s, 1H), 7.15 (s, 1H), 4.07 – 3.78 (m, 2H), 3.10 (d, J = 16.0 Hz, 1H),
690 2.97 (ddd, J = 11.5, 8.0, 3.6 Hz, 1H), 2.84 (d, J = 16.8 Hz, 1H), 2.78 (br s, 2H), 2.00 (d, J = 12.8
691 Hz, 1H), 1.77 (ddd, J = 13.4, 3.9, 1.9 Hz, 1H), 1.66 – 1.50 (m, 1H), 1.46 – 1.40 (m, 1H), 1.38 (s,
692 9H).
693
694 Step 3: To a solution of tert-butyl 4-(4-hydroxy-6-oxo-4-(trifluoromethyl)-4,5,6,7-
695 tetrahydroisoxazolo[5,4-b]pyridin-3-yl)piperidine-1-carboxylate (**7c**, 520 mg, 1.28 mmol) in
696 CH_2Cl_2 (5 ml) was added HCl (4M in dioxane, 10.3 mmol, 2.56 mL, ca. 8 equiv). The mixture

was stirred at RT for 2 h. Then, hexane (15 mL) was added, stirred, and then the hexane solvent was carefully removed (3 times). The solid was then dried in vacuo to give 4-hydroxy-3-(piperidin-4-yl)-4-(trifluoromethyl)-4,5-dihydroisoxazolo[5,4-b]pyridin-6(7H)-one, HCl (**7**, 366 mg, 1.07 mmol, 83 % yield). The product was used without further purification. LC-MS (Method 1): t_R = 2.28 min, m/z $(M+H)^+$ = 306.

Synthesis of 6-(4-(4-Hydroxy-6-oxo-4-(trifluoromethyl)-4,5,6,7-tetrahydro-1H-pyrazolo[3,4-b]pyridin-3-yl)piperidin-1-yl)-4-(trifluoromethyl)nicotinonitrile, TFA (1)

To a solution of 4-hydroxy-3-(piperidin-4-yl)-4-(trifluoromethyl)-4,5-dihydro-1H-pyrazolo[3,4-b]pyridin-6(7H)-one, HCl (**5**, 34.1 mg, 0.1 mmol) in EtOH (2 mL) was added 6-chloro-4-(trifluoromethyl)nicotinonitrile (41.3 mg, 0.20 mmol) and Et_3N (0.042 mL, 0.30 mmol). The mixture was stirred at RT for 1 h and then concentrated to remove most of EtOH. The mixture was dissolved in DMF, filtered through a filter and then submitted for purification by semi-preparative HPLC to give 6-(4-(4-hydroxy-6-oxo-4-(trifluoromethyl)-4,5,6,7-tetrahydro-1H-pyrazolo[3,4-b]pyridin-3-yl)piperidin-1-yl)-4-(trifluoromethyl)nicotinonitrile, TFA (**1**, 7.7 mg, 0.013 mmol, 13.1 % yield). ^{1}H NMR (400 MHz, DMSO-d_6) δ 12.14 (s, 1H), 10.46 (s, 1H), 8.69 (s, 1H), 7.29 (s, 1H), 6.72 (s, 1H), 4.68 (s, 2H), 3.40 – 3.29 (m, 1H), 3.05 (t, J = 12.9 Hz, 2H), 2.87 (d, J = 16.7 Hz, 1H), 2.70 (d, J = 16.5 Hz, 1H), 1.91 (d, J = 11.7 Hz, 1H), 1.73 (d, J = 5.2 Hz, 2H), 1.64 (qd, J = 12.5, 3.8 Hz, 1H); LC-MS (Method 2): t_R = 4.70 min, m/z $(M+H)^+$ = 475.

Synthesis of 4-Hydroxy-4-(trifluoromethyl)-3-(1-(5-(trifluoromethyl)pyrazin-2-yl)piperidin-4-yl)-4,5-dihydro-1H-pyrazolo[3,4-b]pyridin-6(7H)-one (2)

To a solution of 4-hydroxy-3-(piperidin-4-yl)-4-(trifluoromethyl)-4,5-dihydro-1H-pyrazolo[3,4-b]pyridin-6(7H)-one, HCl (**5**, 153 mg, 0.45 mmol) in DMSO (2 mL) was added 2-chloro-5-(trifluoromethyl)pyrazine (123 mg, 0.675 mmol) and then Hunig's base (0.16 mL, 0.90 mmol). The mixture was stirred at RT for 3 h. The mixture was diluted with EtOAc (30 mL), washed with H_2O (30 mL x 2), dried (Na_2SO_4) and filtered. After removal of solvent, the product was purified by silica gel chromatography using 45-85% EtOAc/hexane as the eluent to give 4-hydroxy-4-(trifluoromethyl)-3-(1-(5-(trifluoromethyl)pyrazin-2-yl)piperidin-4-yl)-4,5-dihydro-1H-pyrazolo[3,4-b]pyridin-6(7H)-one (**2**, 155 mg, 0.344 mmol, 76 % yield) as a white solid. ^{1}H NMR (400 MHz, DMSO-d_6) δ 12.15 (s, 1H), 10.46 (s, 1H), 8.48 – 8.46 (m, 2H), 6.72 (s, 1H), 4.62 – 4.58 (m, 2H), 3.38 – 3.31 (m, 1H), 3.08 – 2.96 (m, 2H), 2.87 (d, J = 16.6 Hz, 1H), 2.70 (d, J = 16.6 Hz, 1H), 1.96 – 1.84 (m, 1H), 1.76-1.62 (m, 3H); LC-MS (Method 2): t_R = 4.70 min, m/z $(M+H)^+$ = 451.

Synthesis of 7-Hydroxy-7-(trifluoromethyl)-1-(1-(5-(trifluoromethyl)pyrazin-2-yl)piperidin-4-yl)-6,7-dihydro-1H-imidazo[4,5-b]pyridin-5(4H)-one (3) and 7-(trifluoromethyl)-1-(1-(5-(trifluoromethyl)pyrazin-2-yl)piperidin-4-yl)-1H-imidazo[4,5-b]pyridin-5(4H)-one (8)

To a solution of 7-hydroxy-1-(piperidin-4-yl)-7-(trifluoromethyl)-6,7-dihydro-1H-imidazo[4,5-b]pyridin-5(4H)-one, TFA (**6**, 586 mg, 1.4 mmol) in DMSO (2 mL) was added 2-chloro-5-(trifluoromethyl)pyrazine (511 mg, 2.80 mmol) and then Hunig's base (0.489 mL, 2.80 mmol). The mixture was stirred at RT for 3 h. The mixture was diluted with EtOAc (30 mL), washed with H_2O (30 mL x 2), dried (Na_2SO_4) and filtered. After removal of solvent, to the crude

product was added CH_2Cl_2 (10 mL). The product was filtered and washed with CH_2Cl_2 (2 mL x 3) and dried to give product (315 mg). The filtrate containing some desired product was concentrated and purified by silica gel chromatography using 5-10% MeOH/CH_2Cl_2 to give 163 mg of product. Total, 478 mg of product was obtained. 7-hydroxy-7-(trifluoromethyl)-1-(1-(5-(trifluoromethyl)pyrazin-2-yl)piperidin-4-yl)-6,7-dihydro-1H-imidazo[4,5-b]pyridin-5(4H)-one (**3**, 478 mg, 1.061 mmol, 76 % yield) ^{1}H NMR (400 MHz, DMSO-d_6) δ 10.27 (s, 1H), 8.48 (m, 2H), 7.75 (s, 1H), 7.22 (s, 1H), 4.75 – 4.54 (m, 3H), 3.13 – 2.96 (m, 3H), 2.76 (d, J = 16 Hz, 1H), 2.15 (d, J = 12.3 Hz, 1H), 2.06 (qd, J = 12.4, 4.0 Hz, 1H), 1.93 (d, J = 12.0 Hz, 1H), 1.77 (qd, J = 12.3, 4.1 Hz, 1H); LC-MS (Method 2): t_R = 4.71 min, m/z $(M+H)^+$ = 451. Some elimination side product was also collected and re-purified by silica gel chromatography using 0-5-10% MeOH/CH_2Cl_2 as the eluent to give 7-(trifluoromethyl)-1-(1-(5-(trifluoromethyl)pyrazin-2-yl)piperidin-4-yl)-1H-imidazo[4,5-b]pyridin-5(4H)-one (**8**, 40 mg, 0.093 mmol, 6.6%). ^{1}H NMR (400 MHz, DMSO-d_6) δ 11.89 (br s, 1H), 8.57 (s, 1H), 8.54 – 8.48 (m, 2H), 6.75 (s, 1H), 4.71 (d, J = 13.4 Hz, 2H), 4.46 (q, J = 7.3, 6.9 Hz, 1H), 3.12 (dt, J = 14.3, 8.4 Hz, 2H), 2.16 – 1.95 (m, 4H); LC-MS (Method 2): t_R = 5.02 min, m/z $(M+H)^+$ = 433.

Synthesis of 4-hydroxy-4-(trifluoromethyl)-3-(1-(5-(trifluoromethyl)pyrazin-2-yl)piperidin-4-yl)-4,5-dihydroisoxazolo[5,4-b]pyridin-6(7H)-one (9)

To a solution of 4-hydroxy-3-(piperidin-4-yl)-4-(trifluoromethyl)-4,5-dihydroisoxazolo[5,4-b]pyridin-6(7H)-one, TFA (**7**, 84 mg, 0.2 mmol) in DMF (1 mL) was added 2-chloro-5-(trifluoromethyl)pyrazine (73.0 mg, 0.40 mmol) and Et_3N (0.084 mL, 0.60 mmol). The mixture was stirred at RT for 3 h. The mixture was dropped into a vigorously stirred H_2O (40 mL). The solid was filtered, washed with H_2O (2 x 3 mL) and then dried to give ~ 95 mg of desired

765 product, which is ca. 90-95% purity. The product was dissolved in CH_2Cl_2 and purified by silica
766 gel chromatography using 35-70% EtOAc/hexane as the eluent to give 4-hydroxy-4-
767 (trifluoromethyl)-3-(1-(5-(trifluoromethyl)pyrazin-2-yl)piperidin-4-yl)-4,5-dihydroisoxazolo[5,4-
768 b]pyridin-6(7H)-one (**9**, 42 mg, 0.093 mmol, 46.5 % yield). ^{1}H NMR (400 MHz, DMSO-d_6) δ
769 11.99 (s, 1H), 8.51 – 8.32 (m, 2H), 7.21 (s, 1H), 4.50 (dd, J = 15.5, 12.0 Hz, 2H), 3.23 – 3.05 (m,
770 4H), 2.86 (d, J = 16.8 Hz, 1H), 2.16 (d, J = 12.7 Hz, 1H), 1.92 (d, J = 12.3 Hz, 1H), 1.82 – 1.66
771 (m, 1H), 1.63 – 1.48 (m, 1H); LC-MS (Method 2): t_R = 5.16 min, m/z $(M+H)^+$ = 452.
772
773 **Data Availability**
774 The atomic coordinates and structure factors for crystals of the ΔNΔC-IDFP·**1** complex have
775 been deposited in the PDB with accession code 6DTJ.
776
777 **Competing Interests**
778 The authors declare that they have no competing interests.
779
780 **Acknowledgements**
781 We thank D. J. Leahy (Johns Hopkins University School of Medicine) for the expression vector
782 pProEX HT-EndoH. We also thank the members of the Tesmer lab for their critique of the
783 manuscript.

REFERENCES

MedImmune. A Study to Evaluate the Safety and Efficacy of MEDI6012 in Acute ST Elevation Myocardial Infarction (REAL-TIMI 63B). Available from: https://clinicaltrials.gov/ct2/show/NCT03578809. NLM identifier: NCT03578809.

MedImmune. To Evaluate Safety, Pharmacokinetics and Pharmacodynamics of MEDI6012 in Subjects With Stable Coronary Artery Disease. Available from: https://clinicaltrials.gov/ct2/show/NCT02601560. NLM identifier: NCT02601560.

Adams, P.D., Afonine, P.V., Bunkóczi, G., Chen, V.B., Davis, I.W., Echols, N., Headd, J.J., Hung, L.W., Kapral, G.J., Grosse-Kunstleve, R.W., McCoy, A.J., Moriarty, N.W., Oeffner, R., Read, R.J., Richardson, D.C., Richardson, J.S., Terwilliger, T.C., and Zwart, P.H. (2010). PHENIX: a comprehensive Python-based system for macromolecular structure solution. Acta Crystallographica Section D *66*, 213-221. DOI:10.1107/S0907444909052925

Ahsan, L., Ossoli, A.F., Freeman, L., Vaisman, B., Amar, M.J., Shamburek, R.D., and Remaley, A.T. (2014). Role of Lecithin: Cholesterol Acytransferase in HDL Metabolism and Atherosclerosis. In The HDL Handbook: Biological Functions and Clinical Implications., T. Komoda, ed. (Elsevier), pp. 159-194. ISBN: 978-0-12-407867-3

Calabresi, L., Simonelli, S., Gomaraschi, M., and Franceschini, G. (2012). Genetic lecithin:cholesterol acyltransferase deficiency and cardiovascular disease. Atherosclerosis *222*, 299-306. DOI:10.1016/j.atherosclerosis.2011.11.034

Casteleijn, M.G., Parkkila, P., Viitala, T., and Koivuniemi, A. (2018). Interaction of lecithin:cholesterol acyltransferase with lipid surfaces and apolipoprotein A-I-derived peptides. Journal of lipid research *59*, 670-683. DOI:10.1194/jlr.M082685

Castro-Ferreira, I., Carmo, R., Silva, S.E., Correa, O., Fernandes, S., Sampaio, S., Pedro, R.P., Praca, A., and Oliveira, J.P. (2018). Novel Missense LCAT Gene Mutation Associated with an Atypical Phenotype of Familial LCAT Deficiency in Two Portuguese Brothers. JIMD Rep *40*, 55-62. DOI:10.1007/8904_2017_57

Charlton-Menys, V., Pisciotta, L., Durrington, P.N., Neary, R., Short, C.D., Calabresi, L., Calandra, S., and Bertolini, S. (2007). Molecular characterization of two patients with severe LCAT deficiency. Nephrology Dialysis Transplantation *22*, 2379-2382. DOI:10.1093/ndt/gfm311

Chen, V.B., Arendall, W.B., Headd, J.J., Keedy, D.A., Immormino, R.M., Kapral, G.J., Murray, L.W., Richardson, J.S., and Richardson, D.C. (2010). MolProbity: all-atom structure validation for macromolecular crystallography. Acta Crystallographica Section D *66*, 12-21. DOI:10.1107/S0907444909042073

Chen, Z., Wang, S.-p., Krsmanovic, M.L., Castro-Perez, J., Gagen, K., Mendoza, V., Rosa, R., Shah, V., He, T., Stout, S.J., Geoghagen, N.S., Lee, S.H., McLaren, D.G., Wang, L., Roddy, T.P., Plump, A.S., Hubbard, B.K., Sinz, C.J., and Johns, D.G. (2012). Small molecule activation

821 of lecithin cholesterol acyltransferase modulates lipoprotein metabolism in mice and hamsters.
822 Metabolism *61*, 470-481. DOI:10.1016/j.metabol.2011.08.006

823 Cooke, A.L., Morris, J., Melchior, J.T., Street, S.E., Jerome, W.G., Huang, R., Herr, A.B., Smith,
824 L.E., Segrest, J.P., Remaley, A.T., Shah, A.S., Thompson, T.B., and Davidson, W.S. (2018). A
825 thumbwheel mechanism for APOA1 activation of LCAT activity in HDL. Journal of lipid
826 research *59*, 1244-1255. DOI:10.1194/jlr.M085332

827 Czarnecka, H., and Yokoyama, S. (1996). Regulation of cellular cholesterol efflux by
828 lecithin:cholesterol acyltransferase reaction through nonspecific lipid exchange. Journal of
829 Biological Chemistry *271*, 2023-2028. DOI:10.1074/jbc.271.4.2023

830 J.-L. Dassuex, R. Sekul, K. Buttner, I. Cornut, G. Metz, and J. Dufourcq (1999). Apolipoprotein
831 A-I agonists and their use to treat dyslipidemic disorders. *US Patent No. 6,004,925*.

832 Emsley, P., Lohkamp, B., Scott, W.G., and Cowtan, K. (2010). Features and development of
833 Coot. Acta Crystallographica Section D *66*, 486-501. DOI:10.1107/S0907444910007493

834 Fielding, C.J., Shore, V.G., and Fielding, P.E. (1972). A protein cofactor of lecithin:cholesterol
835 acyltransferase. Biochemical and Biophysical Research Communications *46*, 1493-1498.
836 DOI:10.1016/0006-291X(72)90776-0

837 Freeman, L.A., Demosky, S.J., Jr., Konaklieva, M., Kuskovsky, R., Aponte, A., Ossoli, A.F.,
838 Gordon, S.M., Koby, R.F., Manthei, K.A., Shen, M., Vaisman, B.L., Shamburek, R.D., Jadhav,
839 A., Calabresi, L., Gucek, M., Tesmer, J.J.G., Levine, R.L., and Remaley, A.T. (2017).
840 Lecithin:Cholesterol Acyltransferase Activation by Sulfhydryl-Reactive Small Molecules: Role
841 of Cysteine-31. Journal of pharmacology and experimental therapeutics *362*, 306-318.
842 DOI:10.1124/jpet.117.240457

843 Glomset, J.A. (1968). The plasma lecithins:cholesterol acyltransferase reaction. Journal of lipid
844 research *9*, 155-167.

845 Glukhova, A., Hinkovska-Galcheva, V., Kelly, R., Abe, A., Shayman, J.A., and Tesmer, J.J.
846 (2015). Structure and function of lysosomal phospholipase A2 and lecithin:cholesterol
847 acyltransferase. Nat Commun *6*, 6250. DOI:10.1038/ncomms7250

848 Gunawardane, R.N., Fordstrom, P., Piper, D.E., Masterman, S., Siu, S., Liu, D., Brown, M., Lu,
849 M., Tang, J., Zhang, R., Cheng, J., Gates, A., Meininger, D., Chan, J., Carlson, T., Walker, N.,
850 Schwarz, M., Delaney, J., and Zhou, M. (2016). Agonistic Human Antibodies Binding to
851 Lecithin-Cholesterol Acyltransferase Modulate High Density Lipoprotein Metabolism. Journal
852 of Biological Chemistry *291*, 2799-2811. DOI:10.1074/jbc.M115.672790

853 Hayward, S., and Berendsen, H.J. (1998). Systematic analysis of domain motions in proteins
854 from conformational change: new results on citrate synthase and T4 lysozyme. Proteins *30*, 144-
855 154. DOI:10.1002/(SICI)1097-0134(19980201)30:2<144::AID-PROT4>3.0.CO;2-N

856 Ho, B.K., and Gruswitz, F. (2008). HOLLOW: generating accurate representations of channel
857 and interior surfaces in molecular structures. BMC Struct Biol *8*, 49. DOI:10.1186/1472-6807-8-
858 49

859 Hörl, G., Kroisel, P.M., Wagner, E., Tiran, B., Petek, E., and Steyrer, E. (2006). Compound
860 heterozygosity (G71R/R140H) in the lecithin:cholesterol acyltransferase (LCAT) gene results in
861 an intermediate phenotype between LCAT-deficiency and fish-eye disease. Atherosclerosis *187*,
862 101-109. DOI:10.1016/j.atherosclerosis.2005.08.038

863 Jonas, A. (2000). Lecithin cholesterol acyltransferase. Biochimica et Biophysica Acta.
864 DOI:10.1016/S1388-1981(00)00153-0

865 F. Kayser, M. Labelle, B. Shan, J. Zhang, and M. Zhou (2013). Methods for treating
866 atherosclerosis. *US Patent No. 8,426,358 B2*.

867 Kingwell, B.A., Chapman, M.J., Kontush, A., and Miller, N.E. (2014). HDL-targeted therapies:
868 progress, failures and future. Nature Reviews Drug Discovery *13*, 445-464.
869 DOI:10.1038/nrd4279

870 H. Kobayashi, M. Arai, T. Kaneko, and N. Terasaka (2016). 5-hydroxy-4-
871 (trifluoromethyl)pyrazolopyridine derivative. *US Patent No. 9,796,709 B2*.

872 H. Kobayashi, N. Ohkawa, M. Takano, H. Kubota, T. Onoda, T. Kaneko, M. Arai, and N.
873 Terasaka (2015a). Piperidinylpyrazolopyridine derivative. *US Patent No. 9,150,575 B2*.

874 H. Kobayashi, T. Onoda, T. Kaneko, and K. Ishibashi (2015b). Condensed Pyrazole Derivative.
875 *WO Patent No. 2015111545*.

876 Krissinel, E., and Henrick, K. (2004). Secondary-structure matching (SSM), a new tool for fast
877 protein structure alignment in three dimensions. Acta Crystallographica Section D *60*, 2256-
878 2268. DOI:10.1107/S0907444904026460

879 Kuivenhoven, J.A., Pritchard, H., Hill, J., Frohlich, J., Assmann, G., and Kastelein, J. (1997).
880 The molecular pathology of lecithin:cholesterol acyltransferase (LCAT) deficiency syndromes.
881 Journal of lipid research *38*, 191-205.

882 Laskowski, R.A., and Swindells, M.B. (2011). LigPlot+: multiple ligand-protein interaction
883 diagrams for drug discovery. Journal of Chemical Information and Modeling *51*, 2778-2786.
884 DOI:10.1021/ci200227u

885 Li, D., Gordon, S., and Schwendeman, A. (2015). Apolipoprotein Mimetic Peptides for
886 Stimulating Cholesterol Efflux. In Apolipoprotein Mimetics in the Management of Human
887 Disease, G.M. Anantharamaiah, and D. Goldberg, eds. (New York: Springer International
888 Publishing), pp. 29-42. ISBN: 9783319173504

889 Manthei, K.A., Ahn, J., Glukhova, A., Yuan, W., Larkin, C., Manett, T.D., Chang, L., Shayman,
890 J.A., Axley, M.J., Schwendeman, A., and Tesmer, J.J.G. (2017). A retractable lid in
891 lecithin:cholesterol acyltransferase provides a structural mechanism for activation by

892 apolipoprotein A-I. Journal of Biological Chemistry *292*, 20313-20327.
893 DOI:10.1074/jbc.M117.802736

894 McCoy, A.J., McCoy, McCoy, A.J., and A.J. (2007). Solving structures of protein complexes by
895 molecular replacement with Phaser. Acta Crystallographica Section D *63*, 32-41.
896 DOI:10.1107/S0907444906045975

897 McLean, J.W. (1992). Molecular Defects in the Lecithin:Cholesterol Acyltransferase Gene. In
898 High density lipoproteins and atherosclerosis III: proceedings of the 3rd International
899 Symposium on Plasma High Density Lipoproteins and Atherosclerosis, N.E. Miller, and A.R.
900 Tall, eds. (San Antonio, Elsevier Science Publishers), pp. 59-65.

901 Murshudov, G.N., Skubák, P., Lebedev, A.A., Pannu, N.S., Steiner, R.A., Nicholls, R.A., Winn,
902 M.D., Long, F., and Vagin, A.A. (2011). REFMAC5 for the refinement of macromolecular
903 crystal structures. Acta Crystallographica Section D *67*, 355-367.
904 DOI:10.1107/S0907444911001314

905 T. Onoda, T. Kaneko, M. Arai, H. Kobayashi, and N. Terasaka (2015). Imidazopyridine
906 Derivative. *WO Patent No. 2015087996*.

907 Ossoli, A., Neufeld, E.B., Thacker, S.G., Vaisman, B., Pryor, M., Freeman, L.A., Brantner, C.A.,
908 Baranova, I., Francone, N.O., Demosky, S.J., Jr., Vitali, C., Locatelli, M., Abbate, M., Zoja, C.,
909 Franceschini, G., Calabresi, L., and Remaley, A.T. (2016). Lipoprotein X Causes Renal Disease
910 in LCAT Deficiency. PloS ONE *11*, e0150083. DOI:10.1371/journal.pone.0150083

911 Otwinowski, Z., and Minor, W. (1997). Processing of X-ray diffraction data collected in
912 oscillation mode. Methods in enzymology *276*, 307-326. DOI:10.1016/S0076-6879(97)76066-X

913 Pettersen, E.F., Goddard, T.D., Huang, C.C., Couch, G.S., Greenblatt, D.M., Meng, E.C., and
914 Ferrin, T.E. (2004). UCSF Chimera - a visualization system for exploratory research and
915 analysis. Journal of computational chemistry *25*, 1605-1612. DOI:10.1002/jcc.20084

916 Piper, D.E., Romanow, W.G., Gunawardane, R.N., Fordstrom, P., Masterman, S., Pan, O.,
917 Thibault, S.T., Zhang, R., Meininger, D., Schwarz, M., Wang, Z., King, C., Zhou, M., and
918 Walker, N.P. (2015). The high-resolution crystal structure of human LCAT. Journal of lipid
919 research *56*, 1711-1719. DOI:10.1194/jlr.M059873

920 Pisciotta, L., Calabresi, L., Lupattelli, G., Siepi, D., Mannarino, M.R., Moleri, E., Bellocchio, A.,
921 Cantafora, A., Tarugi, P., Calandra, S., and Bertolini, S. (2005). Combined monogenic
922 hypercholesterolemia and hypoalphalipoproteinemia caused by mutations in LDL-R and LCAT
923 genes. Atherosclerosis *182*, 153-159. DOI:10.1016/j.atherosclerosis.2005.01.048

924 Rader, D.J. (2016). New Therapeutic Approaches to the Treatment of Dyslipidemia. Cell
925 Metabolism *23*, 405-412. DOI:10.1016/j.cmet.2016.01.005

926 Rousset, X., Shamburek, R., Vaisman, B., Amar, M., and Remaley, A.T. (2011). Lecithin
927 cholesterol acyltransferase: an anti- or pro-atherogenic factor? Curr Atheroscler Rep *13*, 249-
928 256. DOI:10.1007/s11883-011-0171-6

929 Rousset, X., Vaisman, B., Amar, M., Sethi, A.A., and Remaley, A.T. (2009). Lecithin:
930 cholesterol acyltransferase--from biochemistry to role in cardiovascular disease. Current Opinion
931 in Endocrinology, Diabetes and Obesity *16*, 163-171.

932 Sampaio, C.T., Maranhao, R., Guerra, A.A., Braga, R.M., Santo, R.M., Testagrossa, L.A., Reis,
933 M.A., Silva, J.A., Carrascossi, H., Onuchic, L.F., Balbo, B.E., Saraiva, L.C., Nakano, H.R.,
934 Amaral, A.G., Costa, E., Watanabe, E.H., Neves, P.D., and Chacra, A.P. (2017). Comprehensive
935 Analysis of the Renal and Systemic Phenotypes Associated with Familial Deficiency of Lecithin-
936 Cholesterol Acyltransferase: a Case Series. In American Society of Nephrology - Kidney Week
937 (New Orleans, LA).

938 Shamburek, R.D., Bakker-Arkema, R., Auerbach, B.J., Krause, B.R., Homan, R., Amar, M.J.,
939 Freeman, L.A., and Remaley, A.T. (2016a). Familial lecithin:cholesterol acyltransferase
940 deficiency: First-in-human treatment with enzyme replacement. Journal of clinical lipidology *10*,
941 356-367. DOI:10.1016/j.jacl.2015.12.007

942 Shamburek, R.D., Bakker-Arkema, R., Shamburek, A.M., Freeman, L.A., Amar, M.J., Auerbach,
943 B., Krause, B.R., Homan, R., Adelman, S.J., Collins, H.L., Sampson, M., Wolska, A., and
944 Remaley, A.T. (2016b). Safety and Tolerability of ACP-501, a Recombinant Human
945 Lecithin:Cholesterol Acyltransferase, in a Phase 1 Single-Dose Escalation Study. Circulation
946 research *118*, 73-82. DOI:10.1161/CIRCRESAHA.115.306223

947 Strom, E.H., Sund, S., Reier-Nilsen, M., Dorje, C., and Leren, T.P. (2011). Lecithin: Cholesterol
948 Acyltransferase (LCAT) Deficiency: renal lesions with early graft recurrence. Ultrastructural
949 Pathology *35*, 139-145. DOI:10.3109/01913123.2010.551578

950 Vrabec, M.P., Shapiro, M.B., Koller, E., Wiebe, D.A., Henricks, J., and Albers, J.J. (1988).
951 Ophthalmic observations in lecithin cholesterol acyltransferase deficiency. JAMA
952 Ophthalmology *106*, 225-229. DOI:10.1001/archopht.1988.01060130235035

953

954

Table 1. EC_{50} values of LCAT variants in esterase and acyltransferase assays

	MUP assay EC_{50} (μM)			DHE assay EC_{50} (μM)
Variant/Cmpd	**1**	**2**	**3**	**2**
WT	0.16 ± 0.01	0.28 ± 0.04	0.32 ± 0.05	0.28 ± 0.09
Y51S	0.59 ± 0.03	0.74 ± 0.2	1.6 ± 0.4	ND
G71I	> 5	> 5	> 5	ND
Y51S/G71I	no effect	no effect	no effect	no effect
R244A	0.13 ± 0.02	0.27 ± 0.04	0.40 ± 0.03	0.76 ± 0.2
R244H	0.16 ± 0.03	0.32 ± 0.03	0.47 ± 0.05	4.6 ± 2

ND = not determined. In the MUP esterase assay, compound was titrated from 0.04 – 9.5 μM, and reactions were performed in triplicate. In the DHE acyltransferase assay, **2** was titrated from 0.004 – 10 μM and reactions were performed three times in triplicate. Values reported are mean ± s.e.m.

960 **Table 2. Fold activation for LCAT variants in the MUP esterase assay.**
961

	Fold activation					
Variant/Cmpd	**1**	**2**	**3**	**6**	**8**	**9**
WT	2.3 ± 0.4	2.3 ± 0.4	2.4 ± 0.4	no effect	3.7 ± 0.9	1.6 ± 0.2
Y51S	1.9 ± 0.2	1.8 ± 0.1	1.9 ± 0.2	no effect	2.8 ± 0.6	1.1 ± 0.07
G71I	1.5 ± 0.4	1.7 ± 0.2	1.5 ± 0.2	no effect	1.2 ± 0.1	0.96 ± 0.01
Y51S/G71I	1.3 ± 0.3	0.99 ± 0.03	1.1 ± 0.06	no effect	1.1 ± 0.07	0.97 ± 0.003
R244A	1.7 ± 0.4	1.9 ± 0.2	1.9 ± 0.2	no effect	3.2 ± 0.8	1.2 ± 0.1
R244H	1.6 ± 0.3	1.8 ± 0.1	1.8 ± 0.1	no effect	2.8 ± 0.6	1.3 ± 0.06

962 Compound was titrated from 0.04 – 9.5 μM, and reactions were performed in triplicate with values reported as mean
963 ± s.e.m.

964 **Table 3. Effect of LCAT mutations and compound 1 on HDL binding**
965

Variant	k_{on} (s^{-1} μM^{-1})	k_{off} (s^{-1})	K_d (μM)
WT	0.10 ± 0.006	0.12 ± 0.008	1.2
WT + **1**	0.11 ± 0.003	0.11 ± 0.004	1.0
Y51S/G71I	0.074 ± 0.02	0.33 ± 0.03	4.5
R244A	0.069 ± 0.003	0.22 ± 0.005	3.2
R244A + **1**	0.017 ± 0.009	0.19 ± 0.01	11
R244H	0.022 ± 0.002	0.40 ± 0.004	18
R244H + **1**	0.035 ± 0.005	0.15 ± 0.007	4.3

966 HDLs were attached to streptavidin tips via biotinylated lipid, then dipped into LCAT without or with 10 μM
967 compound **1**. LCAT was titrated from 0.4 – 2.4 μM, k_{obs} was calculated for each concentration and plotted against
968 concentration. Reactions were performed in triplicate and values are reported as mean ± s.e.m.

969 **Table 4. Data collection and refinement statistics**

970

Data collection	ΔNΔC-IDFP·**1**
Space group	*C*2
Cell dimensions	
a, *b*, *c* (Å)	134.5, 106.7, 117.8
α, β, γ (°)	90.0, 125.5, 90.0
Resolution (Å)	30.0-3.10 (3.15-3.10)[1]
R_{merge}	0.115 (≥1)
I / σ_I	11.1 (1.27)
Completeness (%)	98.9 (100.0)
Redundancy	4.2 (4.2)
$CC_{1/2}$	(0.55)
Refinement	
Resolution (Å)	28.8-3.10
No. reflections	20,413
R_{work} / R_{free}	19.1/23.9
No. atoms	6,197
Protein	5,978
Ligand	183
Water	35
B-factors	73.0
Protein	72.6
Ligand	91.0
Water	38.9
R.m.s. deviations	
Bond lengths (Å)	0.008
Bond angles (°)	1.33
Ramachandran statistics	
Favored	93.8
Allowed	5.1
Outliers	1.1

971 [1]Values in parentheses are for the highest-resolution shell.

Table 5. EC_{50} values of LCAT variants in the MUP esterase assay with **6**, **8**, and **9**.

	EC_{50} (μM)		
Variant/Cmpd	**6**	**8**	**9**
WT	no effect	4.6 ± 0.06	7.7 ± 2
Y51S	no effect	> 10	> 10
G71I	no effect	> 10	no effect
Y51S/G71I	no effect	> 10	no effect
R244A	no effect	> 10	6.2 ± 0.8
R244H	no effect	> 10	7.6 ± 1

Compound was titrated from 0.04 – 9.5 μM, and reactions were performed in triplicate with values reported as mean ± s.e.m.

976 **Figure 1.**

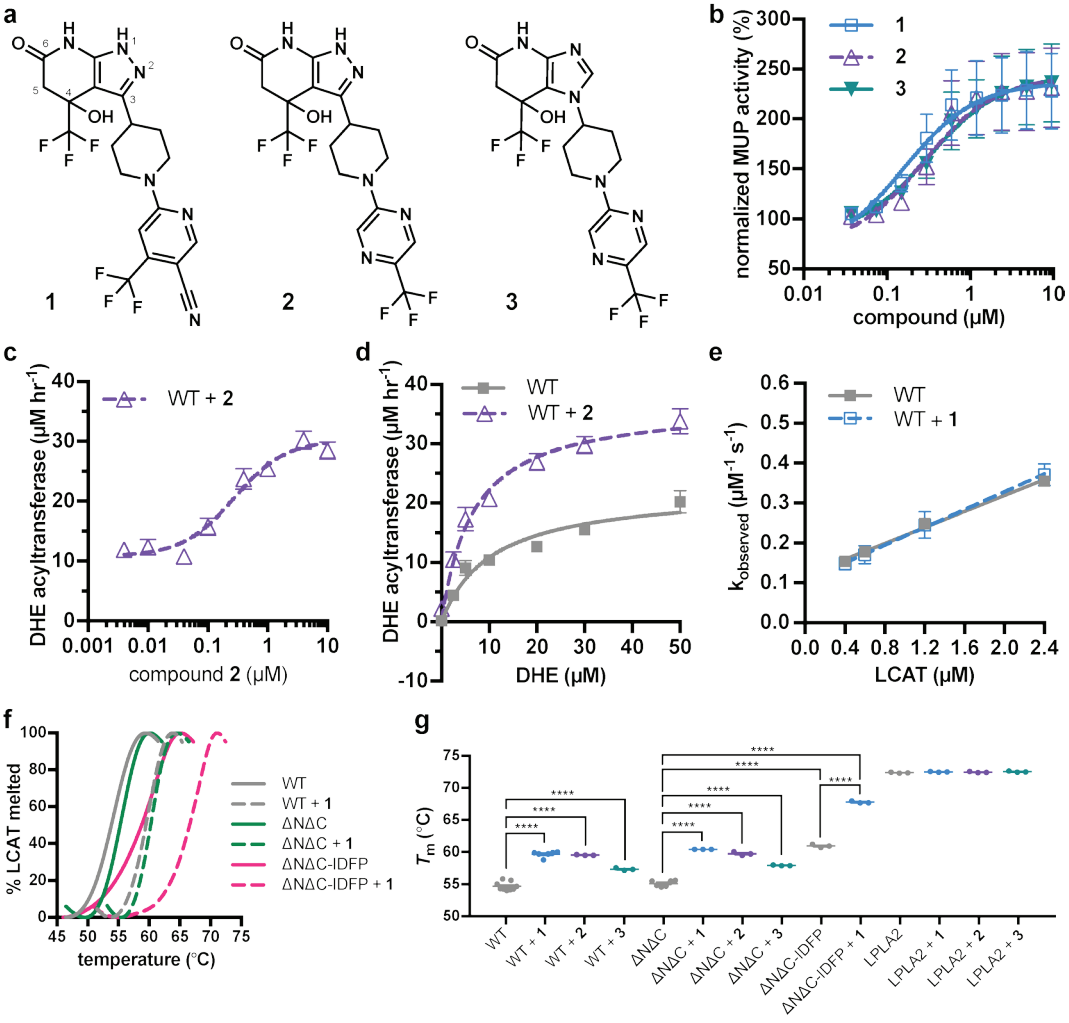

977

978 **Figure 1. Piperidinylpyrazolopyridine and related activators stimulate and stabilize LCAT.** (**a**) Structure of
979 compounds **1** (patent example 95 (Kobayashi et al., 2015a)), **2** (patent example 46 (Kobayashi et al., 2015a)), and **3**
980 (patent example 3 (Onoda et al., 2015)). (**b**) All three activators stimulate LCAT in a micelle-based MUP assay.
981 Data shown are mean ± s.e.m. from three independent experiments, and data were normalized to basal LCAT
982 activity. (**c**) Titration of compound **2,** used in this particular assay due to its lower background fluorescence, in the
983 DHE acyltransferase assay. Data shown are mean ± s.e.m. from three independent experiments performed in
984 triplicate. (**d**) The addition of 5 μM compound **2** stimulates LCAT acyltransferase activity. Data shown are mean ±
985 s.e.m. from three independent experiments performed in triplicate. (**e**) The addition of 10 μM compound **1** does not
986 affect LCAT binding to HDL as measured with BLI. Plot used to determine k_{on}, k_{off}, and hence K_d. Data are mean ±
987 s.e.m. of three independent experiments. (**f**) Representative DSF data highlighting the additive increase in T_m
988 induced by combination of **1** and IDFP. Data are normalized from 0 to 100% using the lowest and highest values,
989 respectively. (**g**) Compounds **1**, **2**, and **3** stabilize WT, ΔNΔC, and ΔNΔC-IDFP LCAT, but not LPLA2. DSF data
990 are mean ± s.e.m. of at least three independent experiments performed in duplicate. **** $P < 0.0001$ by one-way
991 analysis of variance followed by Tukey's multiple comparisons post-test. Each protein without ligand was compared
992 to same variant with ligand, and non-significant pairs are not shown. WT compared to ΔNΔC was not significant.

993 **Figure 2.**

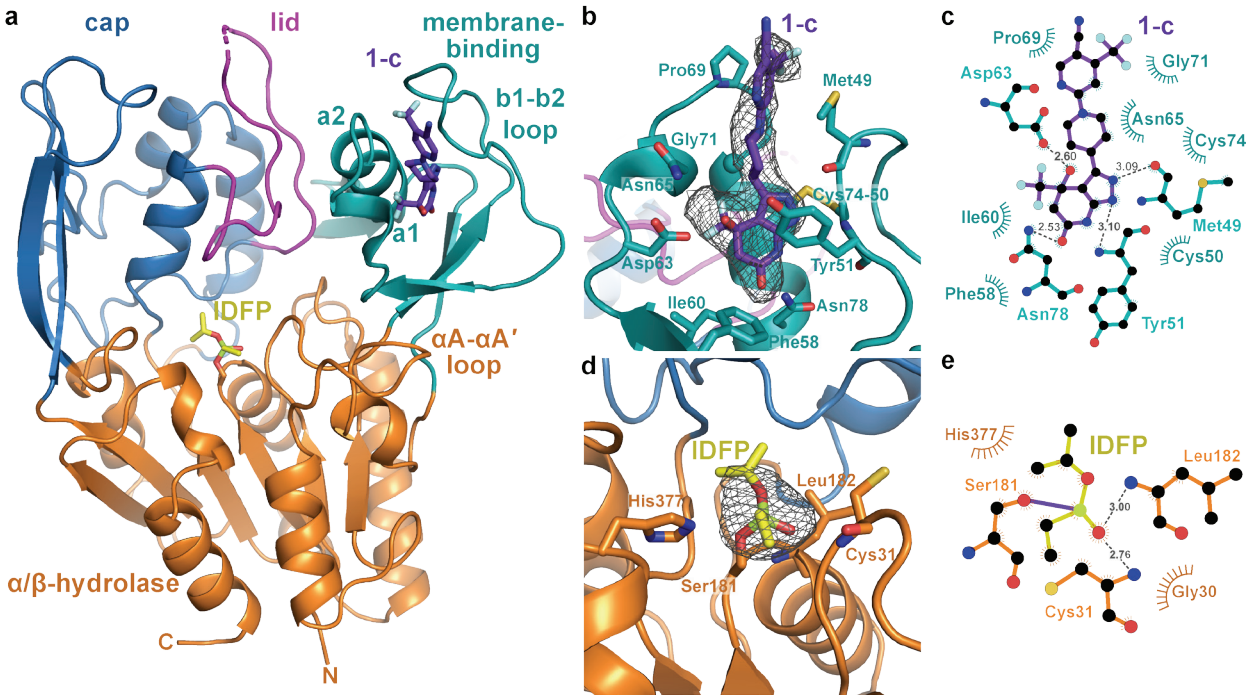

994

995 **Figure 2. Structure of the ΔNΔC-IDFP·1 complex.** (**a**) 3.1 Å X-ray crystal structure highlighting the three
996 domains of LCAT and the binding sites for compound **1-c** (purple, Scheme S1) and IDFP (yellow), shown as stick
997 models. The hydrolase domain is shown in orange, cap domain in blue, lid in magenta, and membrane-binding
998 domain (MBD) in teal. (**b**) Closeup of **1-c** bound to the MBD, with $|F_o|$-$|F_c|$ omit map density contoured at 3 σ in
999 gray mesh. (**c**) LigPlot (Laskowski and Swindells, 2011) of **1-c** bound to LCAT showing interactions between
1000 protein and ligand. Hydrogen bonds are indicated by gray dashed lines with distances in Å. (**d**) IDFP attached to
1001 catalytic Ser181, with $|F_o|$-$|F_c|$ omit map density contoured at 3 σ in gray mesh. (**e**) LigPlot of IDFP bound
1002 covalently to LCAT at Ser181. The covalent point of attachment is indicated by a purple bond. Protein carbons are
1003 colored according to their respective domains or ligands (panel a), whereas nitrogens are blue, oxygens red, sulfurs
1004 yellow, and phosphate lime green.

1005 **Figure 3.**

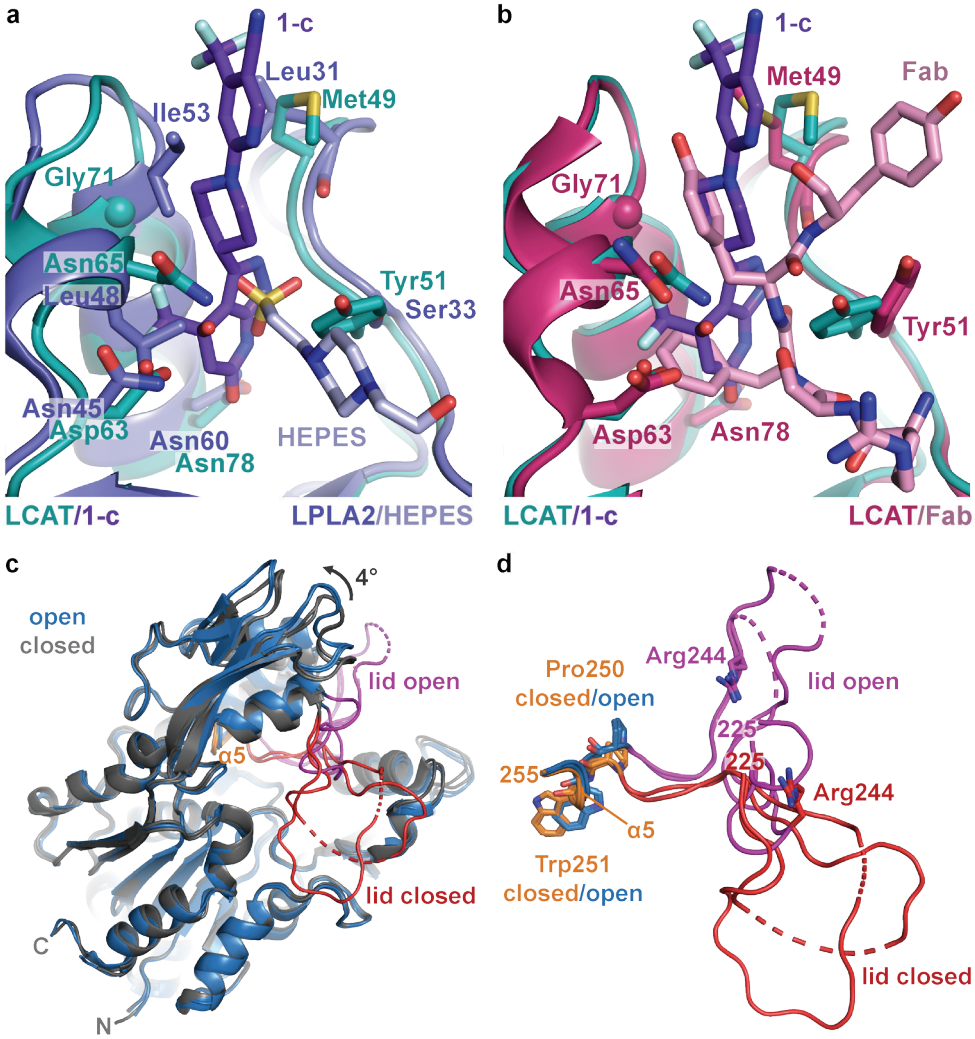

1006

1007 **Figure 3. Comparison of LCAT and LPLA2 structures.** (**a**) ΔNΔC-IDFP·**1** structure aligned with LPLA2 (blue,
1008 PDB entry 4X90) bound to HEPES (light blue). Residues that are not conserved within the binding pocket are
1009 labeled and shown as stick models. (**b**) ΔNΔC-IDFP·**1** structure aligned to the structure of 27C3–LCAT–Fab1 (dark
1010 pink, PDB entry 5BV7 with Fab1 shown in pink), highlighting residues that adjust conformation to accommodate
1011 the different ligands. (**c**) Four LCAT crystal structures aligned to show differences between the open and closed
1012 states. Closed (presumably inactive) structures are shown in gray (PDB entries 4XWG and 5TXF) with orange hinge
1013 and red lid. Open structures (structure reported here and 27C3–LCAT–Fab1) are shown in blue with magenta lid.
1014 Dashed lines indicate disordered residues. (**d**) Close up of structures from (c) only depicting the lid and hinge
1015 region. Hinge residues Pro250 and Trp251 and lid residue Arg244 are shown with stick side chains.

1016 **Figure 4.**

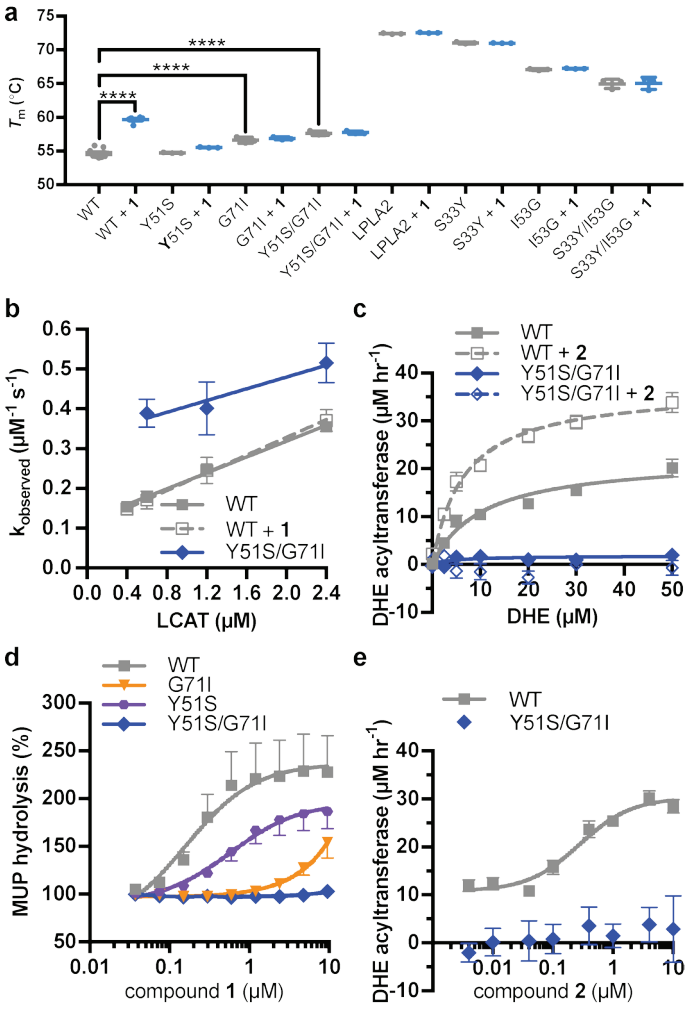

1017

1018 **Figure 4**. **Characterization of activator binding site mutants.** (**a**) Perturbation of the activator binding site leads
1019 to loss of responsiveness to **1**, although the G71I and Y51S/G71I variants are themselves stabilized compared to WT
1020 LCAT. LPLA2 variants, however, do not bind to **1**, and chimeric swaps are destabilized. Data are mean ± s.e.m. of
1021 at least three independent experiments performed in duplicate. **** $P < 0.0001$ by one-way analysis of variance
1022 followed by Tukey's multiple comparisons post-test. Each protein without ligand was compared to that same variant
1023 with **1**, and WT LCAT was compared to each LCAT variant. Non-significant comparisons are not shown. (**b**) Plot
1024 used to determine k_{on}, k_{off}, and hence K_d from BLI data for LCAT binding to HDL. Data are mean ± s.e.m. of three
1025 independent experiments. (**c**) DHE acyltransferase assay with peptide HDLs comparing the absence (solid lines) and
1026 presence (dashed lines) of 5 μM **2**, which was used in this particular assay instead of **1** due to its lower background
1027 fluorescence. Data are mean ± s.e.m. of three independent experiments performed in triplicate. (**d**) Titration of
1028 compound **1** in the MUP hydrolysis assay. Data were normalized to basal activity of 100% for each variant to give
1029 percent activation. Data are mean ± s.e.m. of three independent experiments. (**e**) Titration of **2** in the DHE
1030 acyltransferase assay. Data are mean ± s.e.m. of three independent experiments performed in triplicate.

1031 **Figure 5.**

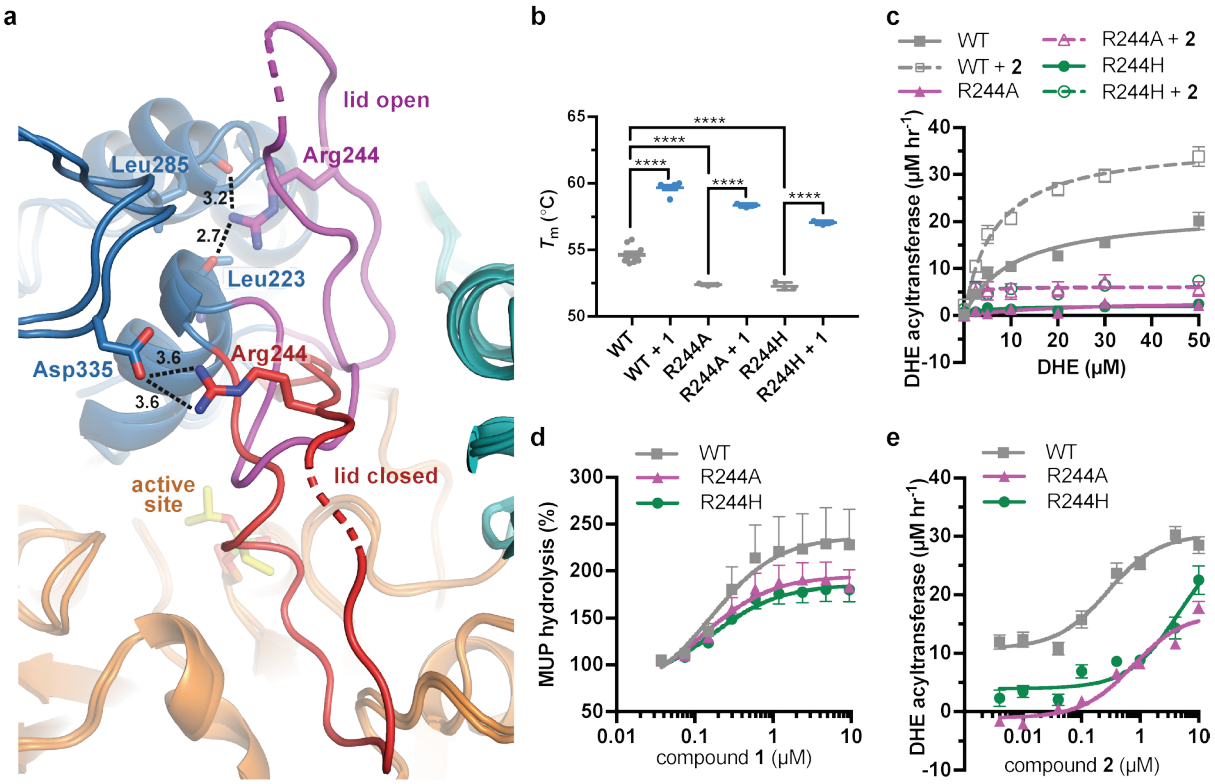

1032

1033 **Figure 5**. **LCAT-Arg244 variants can be partially rescued by LCAT activators.** (**a**) LCAT-Arg244 acts as part
1034 of a molecular switch that interacts with the backbone carbonyls of Leu223 and Leu285 in activated structures of
1035 LCAT (magenta lid). In an inactive structure (red lid, PDB entry 5TXF), Arg244 instead interacts with the side
1036 chain of Asp335. Hydrogen bonds are indicated by black dashed lines with distances in Å. (**b**) The Arg244 variants
1037 have lower T_m values relative to WT, yet **1** can stabilize each to the same extent. Data are mean ± s.e.m. of at least
1038 three independent experiments performed in duplicate. **** $P < 0.0001$ by one-way analysis of variance followed
1039 by Tukey's multiple comparisons post-test. (**d**) DHE acyltransferase assay with peptide-based HDLs comparing the
1040 absence (solid lines) and presence (dashed lines) of 5 μM **2**. Data are mean ± s.e.m. of three independent
1041 experiments performed in triplicate. (**c**) Titration of **1** in the MUP esterase assay. Data were normalized to basal
1042 activity of 100% for each variant to give percent activation. Data are mean ± s.e.m. of three independent
1043 experiments. (**d**) Titration of compound **2** in the DHE acyltransferase assay. Data are mean ± s.e.m. of three
1044 independent experiments performed in triplicate.

1045 **Figure 6.**

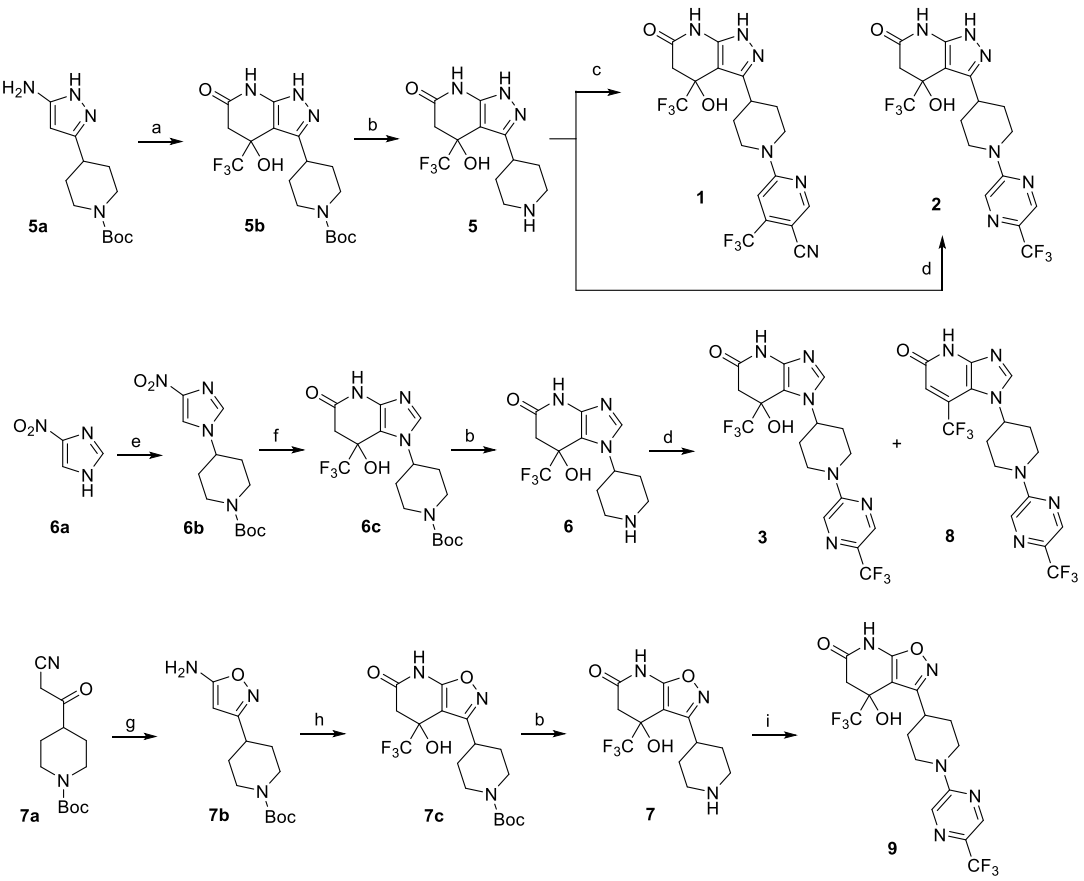

1046

1047 **Figure 6. Synthesis of piperidinylpyrazolopyridine and related compounds.** Reagents and conditions: (a) ethyl
1048 4,4,4-trifluoro-3-oxobutanoate, AcOH, 60 °C, 3 h, 57%. (b) HCl (4 M in 1,4-dioxane), 1,4-dioxane, 0 °C to RT, 2 h,
1049 **5** (96%), **6** (96%), **7** (83%). (c) 6-chloro-4-(trifluoromethyl)nicotinonitrile, Et_3N, EtOH, RT, 1 h, 13%. (d) 2-chloro-
1050 5-(trifluoromethyl)pyrazine, $(i\text{-}Pr)_2NEt$, DMSO, RT, 3 h, **2** (76%), **3** (76%), **8** (~9%). (e) tert-butyl 4-
1051 ((methylsulfonyl)oxy)piperidine-1-carboxylate, K_2CO_3, DMF, 110 °C, overnight, 38%. (f) H_2 balloon, cat. Pd/C,
1052 EtOH, RT, 2.5 h; then ethyl 4,4,4-trifluoro-3-oxobutanoate, EtOH/AcOH (~1:2), 65-70 °C, 2.5 h, 86%. (g)
1053 hydroxylamine HCl salt, Et_3N, CH_2Cl_2, sealed, 55 °C, overnight, 88%. (h) ethyl 4,4,4-trifluoro-3-oxobutanoate,
1054 EtOH/AcOH (~1:2), 70 °C, 6 h, 64%. (i) 2-chloro-5-(trifluoromethyl)pyrazine , Et_3N, DMF, RT, 3 h, 47%.

Figure S1.

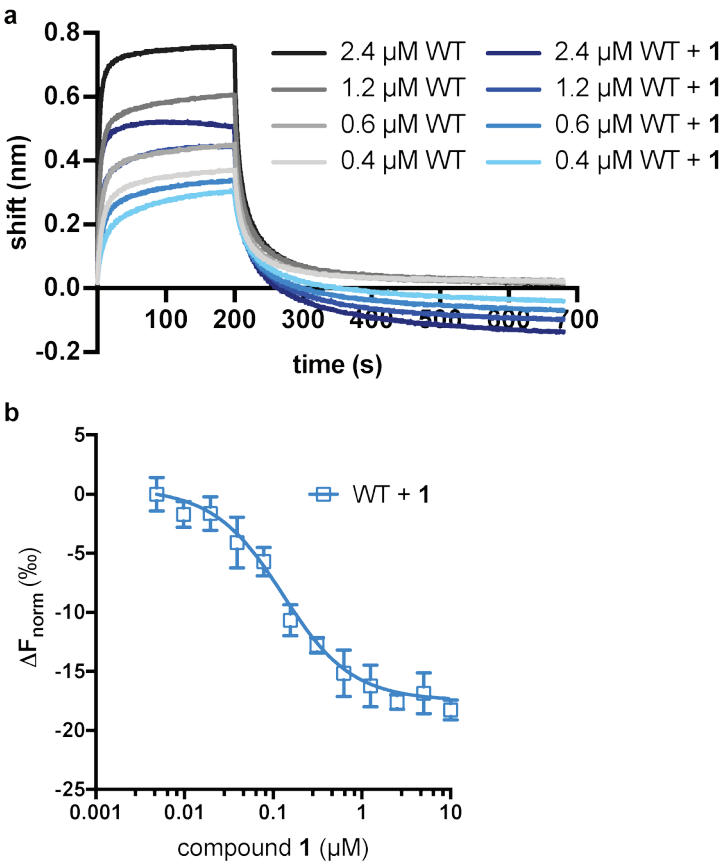

Figure S1. Effects of LCAT binding to compound 1. (**a**) LCAT analyzed with ApoA-I HDLs at different concentrations in order to determine K_d. Raw data with WT LCAT is shown in black to gray, whereas WT in complex with compound **1** is shown in navy to light blue. (**b**) Microscale thermophoresis (MST) data for compound **1** binding to LCAT with a K_d value of 100 ± 14 nM.

Figure S2.

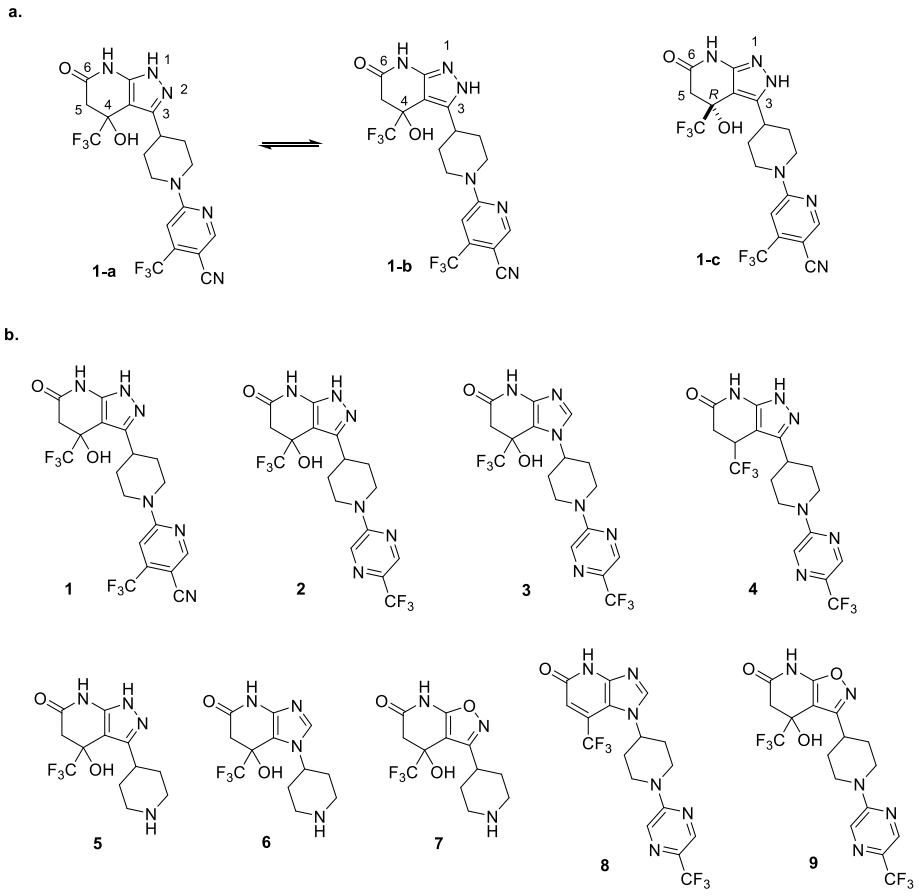

Figure S2. Compound structures and numbers. (**a**) **1-a** and **1-b** are tautomers of **1**, and **1-b** is the dominant isoform in the co-crystal structure. **1** has a stereocenter at the C4 position and was synthesized as a racemic mixture, however the binding site is only compatible with the ***R*** enantiomer, **1-c**. (**b**) Structure of compounds **1** (patent example 95 (Kobayashi et al., 2015a)), **2** (patent example 46 (Kobayashi et al., 2015a)), and **3** (patent example 3 (Onoda et al., 2015)) are the main compounds synthesized and examined in the text. Compound **4** (patent example 10 (Kobayashi et al., 2015b)) is referenced in text. Compounds **5-7** are the head groups of related compounds that were synthesized as intermediates, and **8** and **9** were synthesized as part of the structure-activity relationships.

Figure S3.

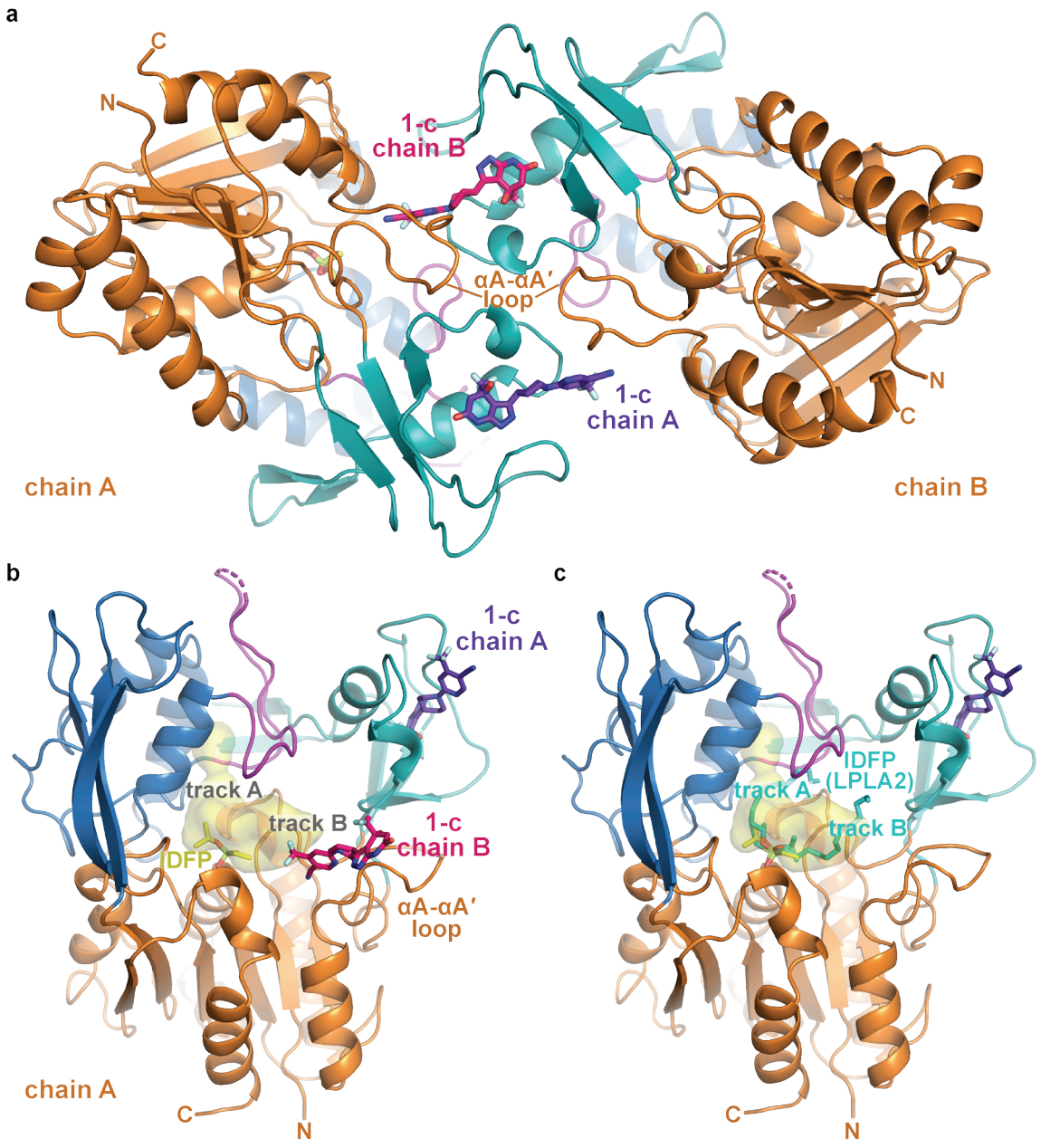

Figure S3. Asymmetric unit of the ΔNΔC-IDFP·1 crystals and interactions of compound 1-c. (**a**) Compound **1-c** helps to bridge the two LCAT chains to form a pseudo 2-fold interface. (**b**) LCAT from chain A is shown with compound **1-c** from both chain A (bound to membrane binding domain, purple) and chain B (docking to track B in the active site, pink). (**c**) For comparison, IDFP from the LPLA2-IDFP structure (PDB entry 4X91 chain A (Glukhova et al., 2015)) is shown with cyan carbons after alignment of LPLA2 and LCAT. IDFP adopts two different orientations in 4X91, thus revealing two potential tracks for acyl chains. The structure shown is of ΔNΔC-IDFP·**1** with bound IDFP (yellow) and **1-c** (purple). The LCAT substrate binding surface is highlighted in yellow. The interior surface showing track A was created using HOLLOW (Ho and Gruswitz, 2008) and rendered in PyMOL. The surface as shown only extends partially into track B because it is designed to show interior surfaces, and track B is more exposed to solvent.

1083 **Figure S4.**

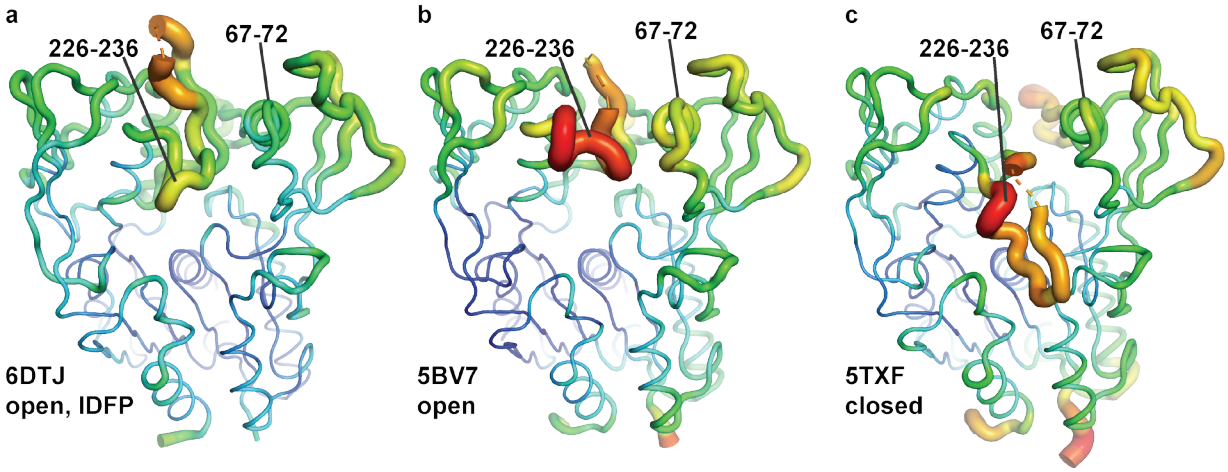

1084

1085 **Figure S4. The ΔNΔC-IDFP·1 structure has lower temperature factors in the membrane binding domain and**
1086 **lid.** (**a**) ΔNΔC-IDFP·**1** open structure, (**b**) 27C3–LCAT–Fab1 open structure (Gunawardane et al., 2016), and (**c**)
1087 LCAT-closed structure (Manthei et al., 2017) are shown using B-factor putty representation in PyMol. The blue to
1088 green coloring and small tube width indicates lower B-factors whereas the yellow to red coloring and wide tube
1089 indicates higher B-factors. Regions with lower B-factors for ΔNΔC-IDFP·**1** are indicated (residues 67-72 and 226-
1090 236), which also had lower hydrogen-deuterium exchange (HDX) in the presence of IDFP (Manthei et al., 2017).

Figure S5.

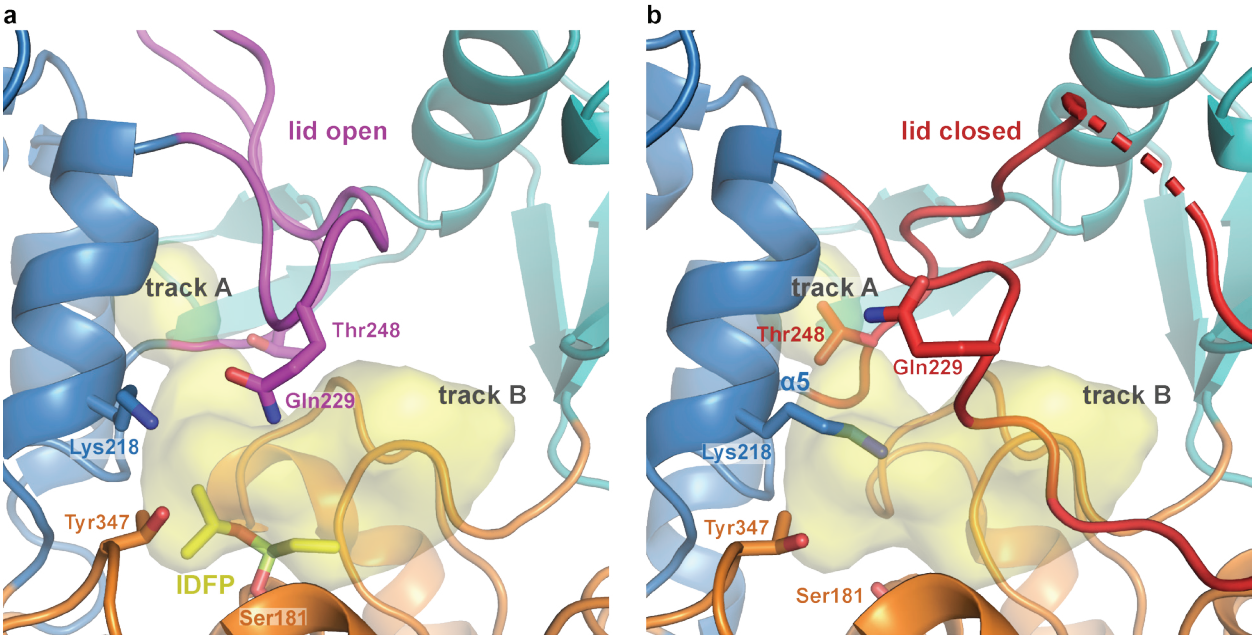

Figure S5. Hinge and lid movement modulate lipid binding tracks. (**a**) When the lid is open, both tracks are fully available for acyl chain binding. Residues Lys218, Gln229, and Tyr347 are in position to coordinate phosphate in the lipid head group. The structure shown is of ΔNΔC-IDFP·**1** with bound IDFP (yellow). The LCAT substrate binding surface is highlighted in yellow. The interior surface showing track A was created using HOLLOW (Ho and Gruswitz, 2008) and rendered in PyMOL. The surface as shown only extends partially into track B because it is designed to show interior surfaces, and track B is more exposed to solvent. (**b**) When the lid is closed, track A becomes blocked by the hinge and lid movement, and specifically the α5 helix causes Thr248 to block the back of track A. Lys218 also occludes part of the binding site and portions of the lid pack in track B. The structure shown is LCAT-closed (PDB code 5TXF (Manthei et al., 2017)).

Figure S6.

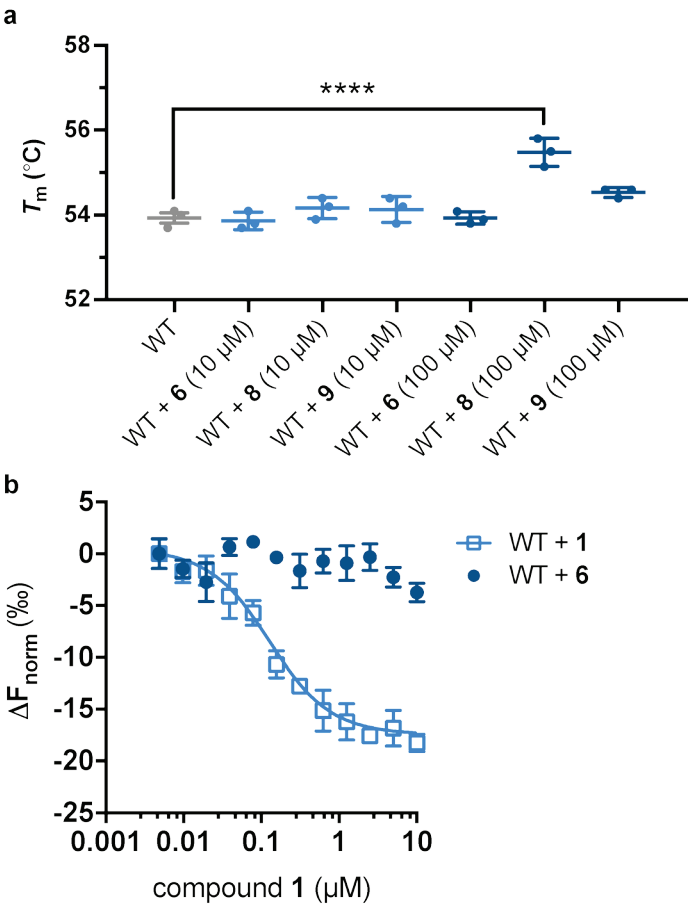

Figure S6. Structure-activity relationships. (**a**) Compounds **6**, **8**, and **9** do not stabilize WT LCAT at 10 µM, but **8** does at 100 µM. Differential scanning fluorescent (DSF) data are mean ± s.e.m. of at least three independent experiments performed in duplicate. **** $P < 0.0001$ by one-way analysis of variance followed by Tukey's multiple comparisons post-test. WT LCAT without ligand was compared to WT with compound and non-significant comparisons are not shown. (**b**) MST data showing that **6** does not bind to WT LCAT, whereas **1** does.

1109 **Figure S7.**

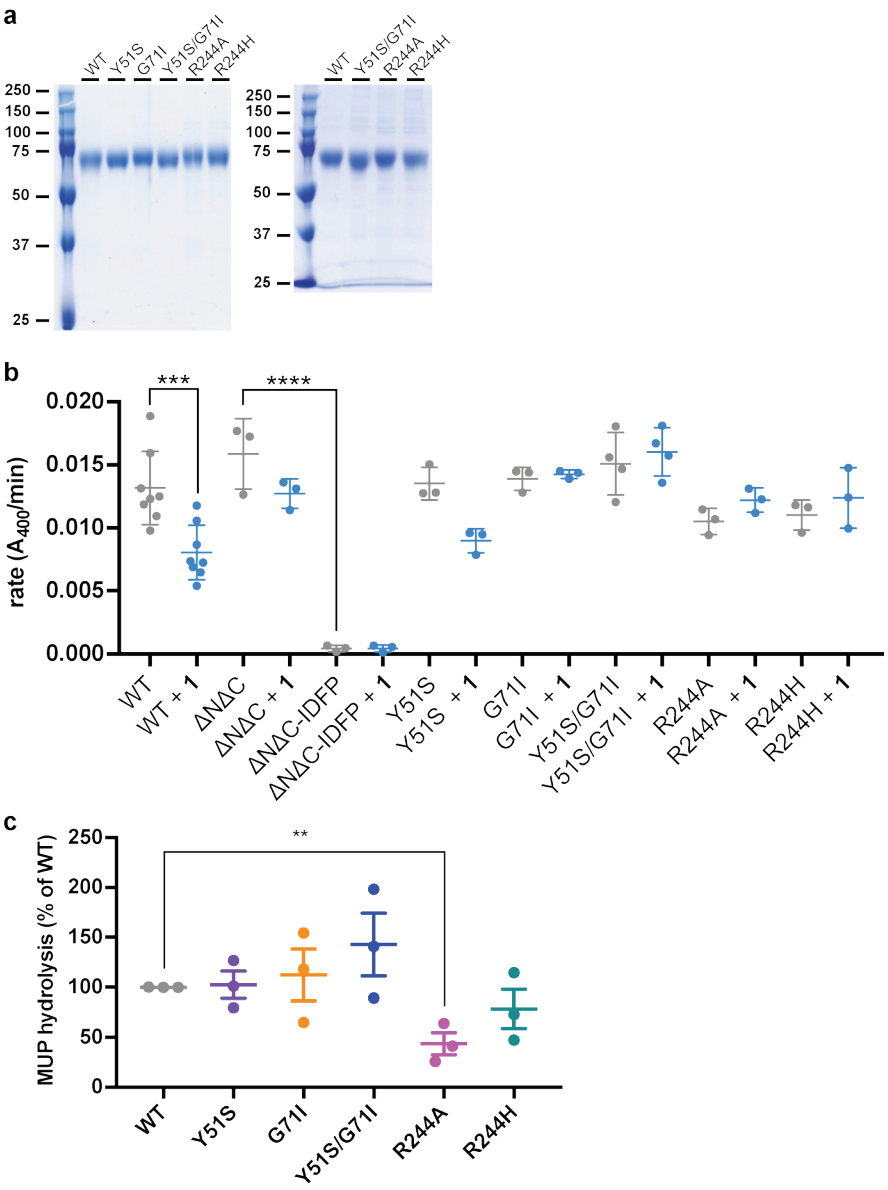

1110

1111 **Figure S7. Biochemical characterization of LCAT variants.** (**a**) SDS-PAGE gels of purified LCAT variants. Left
1112 panel shows representative variants used in pNPB, MUP, and DSF experiments that were polished via Superdex 75.
1113 Right panel shows representative variants used for DHE acyltransferase and BLI assays. Approximately 1.5 µg of
1114 each purified LCAT variant was loaded in each lane. (**b**) Rates of pNPB hydrolysis for LCAT variants. Data are
1115 mean ± s.e.m. of at least three independent experiments. *** $P = 0.0004$, **** $P < 0.0001$ by one-way analysis of
1116 variance followed by Tukey's multiple comparisons post-test. Each protein without ligand was compared to that
1117 same variant with ligand, and WT LCAT was compared to each LCAT variant. Non-significant comparisons are not
1118 shown. (**c**) Comparison of basal MUP hydrolysis. Data are mean ± s.e.m. of three independent experiments
1119 performed with ≥ 27 repeats. ** $P = 0.0070$ by a two-tailed unpaired t test. WT was compared to each LCAT variant
1120 and non-significant comparisons are not shown.

Figure S8.

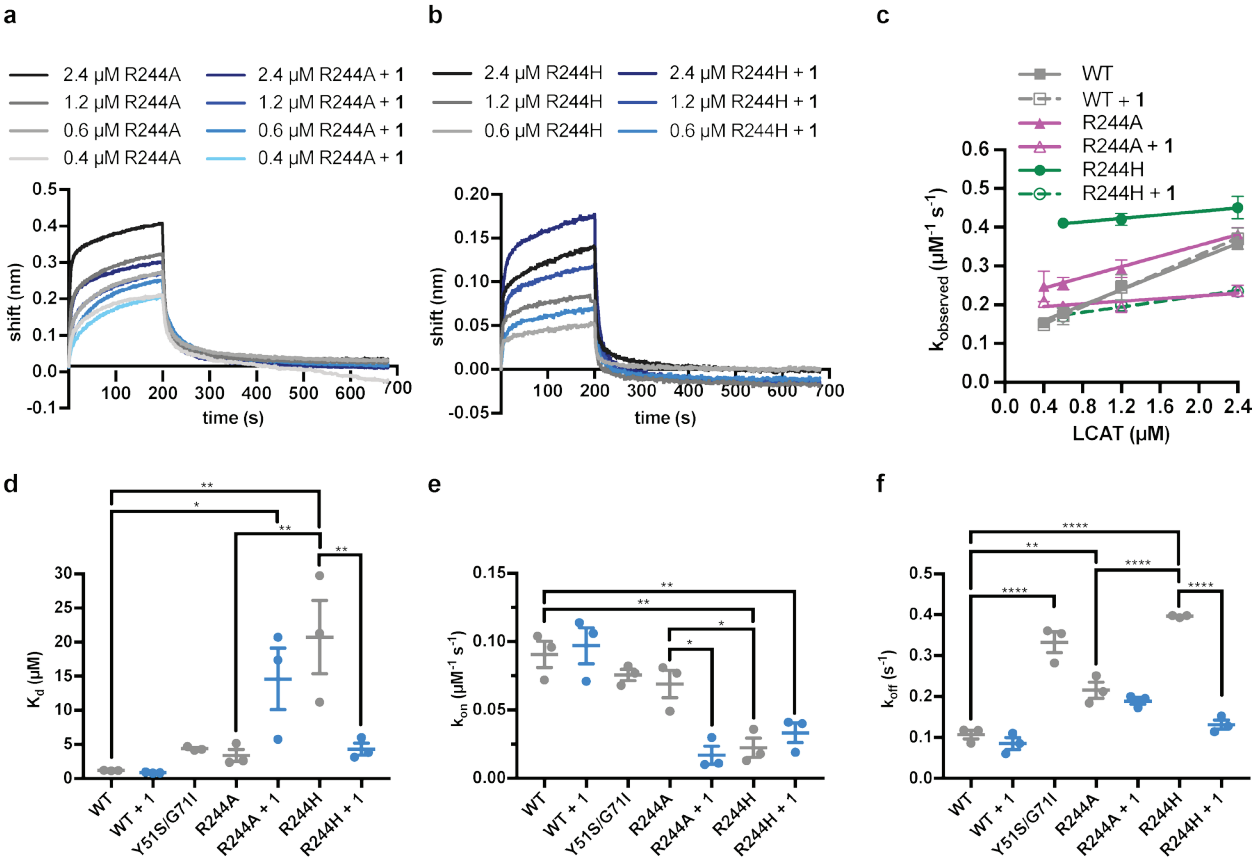

Figure S8. Representative BLI data for LCAT-Arg244 variants. (**a**) LCAT analyzed with ApoA-I HDLs at different concentrations in order to determine K_d. R244A is in black to gray, whereas R244A with compound **1** is in navy to light blue. (**b**) Same as in (a) but with R244H. (**c**) Plot used to determine k_{on} (slope of fit line), k_{off} (y-intercept), and hence K_d for LCAT binding to HDL. Data are mean ± s.e.m. of three independent experiments. (**d**) – (**f**) Individual K_d (**d**), k_{off} (**e**), and k_{on} (**f**) values were calculated for each experiment. Data are mean ± s.e.m. of three independent experiments. * $0.01 < P < 0.05$, ** $0.001 < P < 0.01$, *** $0.0001 < P < 0.001$, **** $P < 0.0001$ by one-way analysis of variance followed by Tukey's multiple comparisons post-test. Each protein without ligand was compared to that same variant with **1**, and WT LCAT was compared to each dataset. R244A was also compared to R244H, and non-significant comparisons are not shown.

Figure S9.

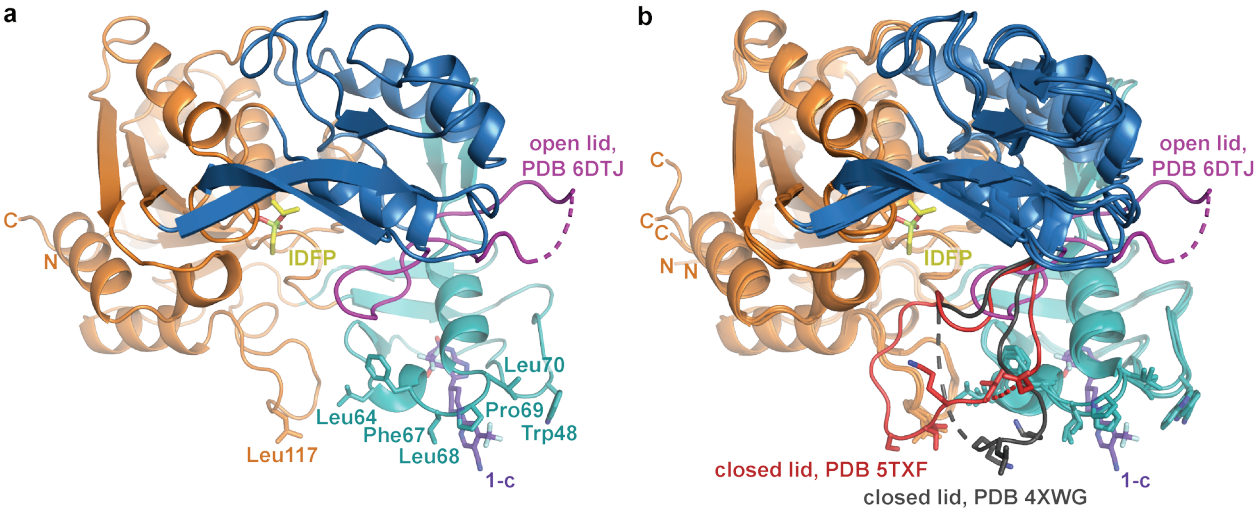

Figure S9. The activator molecule contributes to a hydrophobic surface. (**a**) ΔNΔC-IDFP·**1** oriented so that hydrophobic residues from the membrane binding domain and αA-αA′ loop are all in a plane along bottom of the panel. The pyrazine ring of **1** (purple sticks) also contributes to this plane. The active site lid is shown in magenta. (**b**) When the lid closes, this interface is partially blocked. The lid from PDB entry 5TXF is shown in red (Manthei et al., 2017), and that of PDB entry 4XWG is shown in gray (Piper et al., 2015).

Movie S1. Transition between closed and open conformations of LCAT. The movie highlights the opening of the lid and corresponding cap domain movements that occur upon LCAT activation. Arg244 and the residues it interacts with in each conformation, as well as the active site location Ser181 are shown as sticks. Chimera (Pettersen et al., 2004) was used to morph from the closed structure (PDB entry 5TXF (Manthei et al., 2017)) to the activator structure. The movie was rendered using PyMOL.

Movie S2. Movement corresponding to the hinge region. The same morph as depicted in Movie S1, but zoomed in on the lid and hinge region. The closed (presumably inactive) structure (PDB entry 5TXF (Manthei et al., 2017)) is shown with orange hinge and red lid. The ΔNΔC-IDFP·**1** structure is shown in blue with magenta lid as well as the morph. Dashed lines indicate disordered residues. Hinge residues Pro250 and Trp251 are shown with stick side chains, as well as Arg244 in the lid region. The position of the Cα atom of Gly230 is indicated with a sphere.